Highly loaded magnetocaloric composites by La(Fe,Si)13H powder dedicated to extrusion-based additive manufacturing applications

K.D. N'Dri, N. Charpentier, Laurent Hirsinger, A. Gilbin, T. Barriere

Powder Technology, Vol. 425, July 2023, pp. 118616-1 to 18 (DOI : 10.1016/j.powtec.2023.118616)

Highly loaded magnetocaloric composites by $La(Fe,Si)_{13}H$ powder dedicated to extrusion-based additive manufacturing applications

K.D. N'dri [a], N. Charpentier [a], L. Hirsinger [a], A. Gilbin [b*], T. Barriere [a]
[a] Université de Franche-Comté, CNRS, Institut FEMTO-ST, F-25000 Besançon, France
[b] SUPMICROTECH, CNRS, Institut FEMTO-ST, F-25000 Besançon, France

Abstract

Additive manufacturing is attracting increasing interest in the field of magnetic refrigeration to solve the problem of the brittleness of magnetocaloric alloys. The formulation of a composite based on a thermoplastic binder loaded with $La(Fe,Si)_{13}H$ magnetocaloric powder and then its shaping by an innovative additive manufacturing process were investigated in this work. To best preserve the magnetocaloric properties of the powders, the composite must have the highest powder mass fraction and the most suitable rheological behaviour for 3D printing from pellets. The thermo-rheological characterizations of the powders, the constituents of the binders, the binders and the composites were performed. Except for the powder, these behaviours were modelled as a function of the powder's shear rate, temperature and volume fraction leading to the identification of their different parameters. Criteria encompassing more parameters are defined to select the formulation of the composite with its forming parameters (i.e. from its elaboration to its printing). They lead to the selection of a powder, binder and composite components as well as some process parameters that can be optimised (e.g. maximum powder loading rate, nozzle temperature, shear rate). Particular attention is paid to the homogeneity of the composite and the non-degradation of the magnetocaloric properties throughout the fabrication process (i.e. the preservation of hydrogen in the $La(Fe,Si)_{13}H$ powder) which places this work in the context of 4D printing. Different parts (small 0.6 mm thick plates and characterisation samples) of highly charged magnetocaloric powder (89 % by mass) were printed. Their characterization reveals favourable properties, such as a porosity of 10.8 ± 2 % present in the binder (and a global porosity of 5.4 ± 1 % in the composite) in the form of pore size less than 2.10^{-3} mm^3 and with a few voids of 4.10^{-3} mm^3 obtained by X-ray tomography, and, high magnetocaloric properties (Δs = 9.3 $J \cdot K^{-1} \cdot kg^{-1}$). Other characterizations reveal less favourable mechanical properties, such as a yield strength of 0.7 MPa at room temperature which is highly dependent on the latter rising to an acceptable level of 5 MPa at -20 °C. A comparison with extruded strips of the composite of the same formulation but with lower porosity (i.e. 4% in the binder and overall 2% in the composite) shows an approximately 5-fold

higher yield strength and the same initial Young's modulus, which determines the gap for improvement of the overall printing process used in this study.

Keywords: Thermoplastic composites, Rheological behaviour, 4D printing, Magnetocaloric powders, Extrusion-based additive manufacturing, Additive manufacturing

1. Introduction

Mezaal et al. [1] compared conventional gas compression with magnetic refrigeration, showing that the latter is innovative and promises a greener impact with a higher cooling capacity. Franco et al. [2] studied the MagnetoCaloric Effect (or MCE) of magnetocaloric materials for refrigeration devices and particularly LaFeSiH and NiMnCoIn alloys. Other materials such as $MnFeP_{1-x}As_x$ exhibit exploitable magnetocaloric properties but contain toxic elements [3]. Gadolinium is a reference material for scientific research but it is sensitive to corrosion and too expensive for industrial applications. LaFeSi alloys exhibit a giant magnetocaloric effect ($\Delta s \approx 20\ J \cdot K^{-1} \cdot kg^{-1}$) and use cheap alloying elements such as Fe and Si [4]. The main difficulty is their elaboration because of their mechanical characteristics [5] but the gas atomisation process facilitates the production of high-quality powders [6]. Yang et al. [7] successfully produced $La(Fe,Si)_{13}H$ plates by the hybrid mixing of raw $La(Fe,Si)_{13}$, $MgNiYH_x$ powder, and $Sn_3Ag_{0.5}Cu$.

For magnetic applications, these powders are embedded in thermoplastic polymer binders to produce functional composites [8]. This mixing process helps achieve the desired magnetic properties (for a high volume fraction of powder), extruded materials, mechanical behaviour (e.g. elasticity and ductility) and obtain thermoplastic processable composite materials for processes such as Extrusion-based Additive Manufacturing (or EAM). Polymeric EAM comprises two different processes: Fused Filament Fabrication (or FFF) and Fused Granular Fabrication (or FGF). Rane et al. [9] demonstrated the advantages of the FGF process over the FFF process. In FFF, the filament is driven by motor wheels and is under shear and compression stresses as well as buckling. These effects should be minimised to avoid filament warping [10]. With the composites, it is difficult to fabricate filaments with suitable mechanical properties. In FGF, the pellets are introduced in an extrusion screw, heated, and extruded through the nozzle by screw rotation. Pellets do not require a particular elasticity or strength because they are not mechanically stressed like a filament. Based on these analyses, FGF is more suitable for composite materials and does not require filament elaboration. Rane et al. [11] showed that alumina feedstock printing by FGF resulted in a low porosity value in the final 3D-printed component.

The support required for printing complex parts by EAM significantly increases the consumption of materials, energy, and time. Jiang et al. [12] investigated different strategies to realize this support. Jiang et al. [13] experimented with optimizing its structure in EAM for complex parts. These support systems were considerably reduced, as well as, the material required (by about 30 %), the energy consumption (by 12 %) and the manufacturing time by 7.5 %.

To preserve the high magnetocaloric properties of the LaFeSiH alloy, the process temperature must not exceed the dehydrogenation temperature (~ 453 K for this alloy). Palmero et al. [14]

manufactured an EAM permanent magnet composite with similar temperature limitations. The material processing temperature is set according to the retained magnetocaloric material and reduces the thermal stresses that may occur in the printed part [15]. PolyLactic Acid (or PLA) is a standard material for virgin polymer additive manufacturing and can cope with LaFeSiH temperature limitations. Chaunier et al. [16] reported some conditional specificity with PLA, such as rigidity (characterised by Young's modulus of the material), which must be greater than 1 GPa at ambient temperature, and the melting temperature which must be lower than the printing temperature. Schirmeister et al. [17] performed high-quality EAM without any major deformation and low porosity level from a Low-Density PolyEthylene (or LDPE) filament.

To obtain an appropriate high-loaded composite, it is necessary to incorporate different constituents to improve the specific rheological behaviour. The binder formulation typically includes three main constituents: a primary binder, a lubricant, and a surfactant. The primary binder ensures the cohesion of all elements in the composite comprising the polymeric backbone. The lubricant enables the flow behaviour to be adapted for the selected forming process. The surfactant facilitates the wettability of powder with the other constituents, thus enabling better mechanical adhesion between all components in the compound [18]. Hnatkova et al. [19] used Stearic Acid (or SA) as the surfactant in a binder formulation with ceramic powder. They observed that this addition decreased the shear viscosity of the mixture and enabled a high-volume fraction of powder (~ 60 vol.%). SA enhances the interfacial adhesion of particles due to their high wettability [19]. Ethylene Vinyl Acetate (or EVA) have been investigated to provide elasticity in composites and particularly in the extrusion process [20]. Lanzarini et al. [21] obtained $La(Fe,Si)_{13}H$ microstructured strips using an extrusion process with LDPE, EVA, and SA.

In this work, the shaping by FGF of a magnetocaloric regenerator based on polymer binders (LDPE or PLA + EVA + SA), highly loaded with $La(Fe,Si)_{13}H$ powders was investigated. In section 2, the physical and rheological properties of the two batches of $La(Fe,Si)_{13}H$ powders available were characterised using a powder rheometer. The melting temperatures of the constituents of the binders and the dehydrogenation one of the powders were measured by Differential Scanning Calorimetry (or DSC). They allowed us to determine the temperature for producing the composite and for shaping it. The different methods used for the rheological characterization of the constituents, the elaboration of the composite, its shaping by 3D printing and the mechanical characterization of printed samples are also presented. In section 3, one of the two available powder batches is selected from the Additive Manufacturing Suitability (or AMS) indicator and the critical solid powder loading (or CSL) level in the two formulated composites is determined by two different methods. The choice of the formulation of the composite that incorporates the highest volume fraction of

powder is then made for the rest of this work. The choice of the printing parameters of the composite, such as its shear rate and its nozzle temperature, are justified in Appendix B. A third method is then presented to refine and confirm the highest powder loading in the F1 composite. In section 4, a Rheological AMS (or RAMS) indicator is introduced to confirm the choice of the formulation of the F1 composite as being the best suited for the elaboration and 3D printing processes. To validate the entire process, a functional magnetocaloric printed small plate was shaped with a Direct3D printer, and, various homogeneity and porosity studies by X-ray tomography as well as back scattering SEM images of a clean cross-section obtained by FEMTO-second laser cutting of these printed plates were performed. In section 5, the characterization of the magnetocaloric properties is performed in order, on the one hand, to quantify them for the composite highly loaded with magnetocaloric powder and then, on the other hand, to verify that those of the powder have not been affected by the process for producing the composite and shaping it. Finally, a characterization of the mechanical properties of the final printed composite parts and a comparison with the same formulation of extruded parts are performed to know their respective mechanical limits to consider applications.

2. Materials and methods

2.1. Properties of the magnetocaloric powders

In this study, two batches of $La(Fe,Si)_{13}H$ powder (hereinafter referred to as powders 1 and 2) were supplied by the ERASTEEL company and obtained by gas atomisation using the process described in a previous report [22]. These powders were treated under argon before annealing at 1373 K to form the $NaZn_{13}$ phase which captures the hydrogen atoms and thus controls the phase transition temperature of the powder [23]. Following thermal treatment, powders 1 and 2 have phase transition temperatures of 290 K and 284 K, respectively, and a dehydrogenation temperature of 453 K [21].

Particle size distribution is an important parameter that can strongly affect the properties of manufactured parts and their geometrical shapes. Kukla et al. [24] investigated the effect of particle size on the printing suitability and also noticed that it had an impact on their rheology. The slope of the particle size distribution S_w, which is defined by Eq. (1), predicts the flow behaviour of the feedstock [25]. For example, a S_w value greater than 4 makes it difficult to obtain a defect-free part by the metal injection moulding process.

$$S_w = \frac{2.56}{log(d_{90}/d_{10})} \quad (1)$$

where d_{10} and d_{90} are the particle sizes for the cumulative volumes of 10 % and 90 %, respectively, and the number 2.56 represents the standard deviation of a Gaussian distribution between d_{10} and d_{90}.

Laser diffraction was used to measure the powder particle size distribution using the liquid dispersion method. The powder characteristics are listed in **Table 1**. The unimodal particle size distribution is observed with fine particles (d_{10}) with a value of 7.81 µm and larger particles (d_{90}) placed at ~ 100 µm (powder 1). As shown in this table, the median values (d_{50}) of powders 1 and 2 are 11.90 and 8.91 µm, respectively, which are suitable sizes for extrusion processes for shaping composite filaments (the nozzle diameter used was 0.8 mm). The S_w values of powders 1 (2.25) and 2 (1.81) were less than 4. These results indicated a wide particle size distribution and predicted medium flow behaviour [26]. As the particles of powder 2 are slightly finer than those of powder 1, the powder-filled composite made with the same binders will have a higher shear viscosity with powder 2 than with powder 1 according to [27].

Table 1

$La(Fe,Si)_{13}H$ powder characteristics (where d_x is particle sizes for the cumulative volume of X %).

Powder	d_{10} **(µm)**	d_{50} **(µm)**	d_{60} **(µm)**	d_{90} **(µm)**	S_w **(1)**	**Standard** T_{tr} **(K)**	**Density (g·cm^{-3})**
Powder 1	7.81	11.90	13.12	106.89	2.25 ± 0.02	290 ± 1	6.24
Powder 2	3.90	8.91	11.55	100.17	1.81 ± 0.01	284 ± 1	6.24

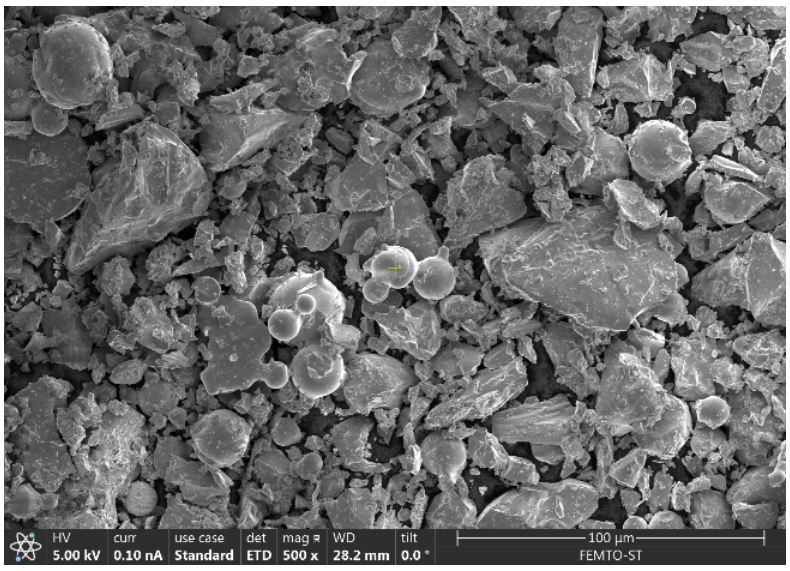

Fig. 1. Morphology of powder 1 obtained by SEM analysis.

Scanning electron microscopy (or SEM) analysis with the ASTM E2142-08 standard was used to analyse the powder morphology. **Fig. 1** presents the analysis of powder 1 and clearly shows two different types of particles. On the one hand, fine and spherical particles are obtained directly from the atomisation process and can agglomerate by collision with each other during the atomisation process. On the other hand, larger particles have been partially or entirely fragmented during the milling process.

2.2. Properties of the different constituents chosen for the binders

To avoid powder dehydrogenation and thus retain its magnetocaloric properties, the printing processes for powder-based magnetocaloric composites require a low melting temperature, T_f [28]. To develop the composite and extrude the parts, Lanzarini et al. [21] used a mixture of LDPE as a polymer binder and SA as a surfactant. In general, EVA is used to provide elasticity during the melting of the extrusion mixture. In addition, for 3D printing, the most commonly used plant-based plastic is PLA. Therefore, the main constituents used as binders in this study are LDPE, PLA, EVA, and SA.

DSC analysis was performed with a DSC 131 evo (SETARAM, Lyon, France) according to the ASTM D3418 standard to determine the thermal properties of the binder constituents. Their main physical characteristics are presented in **Table 2**. The temperature at which the composite was extruded and formed was determined from these data. It must enable the binder to melt while maintaining the functional properties of the magnetocaloric powder. It is therefore between the highest binder melting temperature and the lowest temperature between the binder degradation one and the powder dehydrogenation one [25].

Table 2

Main physical characteristics of binder constituents.

Constituent	Function requested	Melting temperature (K)	Degradation temperature (K)	Helium density ($g \cdot cm^{-3}$)
LDPE	Primary	385 ± 1	533 ± 1	0.61 ± 0.01
PLA	Primary	426 ± 1	562 ± 1	1.25 ± 0.01
EVA	Secondary	325 ± 1	493 ± 1	0.64 ± 0.01
SA	Surfactant	341 ± 1	453 ± 1	0.70 ± 0.01

2.3. Rheological characterization method

The rheological behaviour of the binder constituents is also studied because the knowledge of their fluidity allows the most appropriate shaping process to be chosen. For example, a highly fluid

polymer is suitable for the injection moulding process, and a highly viscous polymer is more suitable for an extrusion process [21].

The rheological behaviour of virgin (i.e. not recycled) PLA, LDPE, EVA, and SA, binders (1 and 2), and formulated composites were measured using a capillary rheometer. Each material sample was conditioned at the test temperature for 5 min in a barrel to ensure temperature homogeneity. The piston speed is controlled to impose shear rates typical for the study of polymers, that is, between 10^2 and 10^4 s^{-1} [29]. Polymers and composites exhibit non-Newtonian flow characteristics, so the Rabinowitsch–Weissenberg correction is applied [30]. The results of shear viscosity versus shear rate and temperature were obtained from the averages of five successive tests and are presented and modelled in Section 0.

2.4. Methods for the elaboration and shaping of composites

The formulations of the binders and composites given in **Table 3** are defined from the physical characteristics of binder constituents presented in **Table 2**. The composition of the F1 composite comes from previous work by Lanzarini for the extrusion of thin sections highly loaded with magnetocaloric powder [31-33]. The composition of the F2 composite is the same as that of the F1 composite but with PLA instead of LDPE to allow the 3D printing of thin strips for the same application.

Table 3

Binders and composites formulations and their processing temperatures.

Binder formulations

Formulation	Composition (vol.%)	Mixing temperature (K)
Binder 1	47.5% LDPE + 47.5% EVA + 5% SA	403
Binder 2	47.5% PLA + 47.5% EVA + 5% SA	443

Composite formulations

Formulation	Composition	Mixing temperature (K)	Printing temperature (K)
F1 composite	Binder 1 + Powder 1	403	403 to 433
F2 composite	Binder 2 + Powder 1	443	

The mixing and printing temperatures, presented in **Table 3**, were selected close to the middle of the temperature range identified in **Table 2**, i.e. between 385 and 453 K for an LDPE-based binder (binder 1), and between 426 and 453 K for a PLA-based binder (binder 2). When powder batch 1 is mixed with one of the two binders (1 or 2), a composite formulation is obtained, hereinafter referred to as F1 (with binder 1) or F2 (with binder 2).

2.4.1. Mixing methods of binders and composites

The binder was mixed with the powder using a twin-screw mixer (Plastograph EC W50EHT) which consists of a vessel with a maximum volume of 50 cm^3 and two counter-rotating screws whose speed is adjustable and was set at 30 rpm for this study. This mixer is also well suited for the manufacture of highly powdered composites [34].

The introduction of mater into the mixer chamber causes a sudden increase in mixing torque and, then, a slow decrease of it with mixing time, which shows an increase in the fluidity and homogeneity of the mixture [19]. Of course, the shear viscosity of the mixture also contributes to increasing this mixing torque [35], but, the homogeneity of the mixing is achieved when its torque stabilises at a final constant value [21] which is measured in this study with an error of 0.7 N·m.

The critical solid powder loading (or CSL) in a composite is the maximum volume fraction of powder that can be incorporated into the polymer binder of that composite while maintaining a homogeneous mixing. To experimentally determine this CSL, the first method presented in section 3.2 consists of introducing the powder in small quantities several times (i.e. incrementally) into the same mixture whose powder concentration increases regularly, whereas a second method, presented in section 3.3, consists of making a single mixture per concentration by introducing the powder at once into its binder. A more precise determination of the CSL by a third method is made in section 0 by measuring the shear viscosity of the composite followed by an identification of this viscous behaviour by a model of the power-law type. The search for the discontinuity of this pseudo-plasticity exponent, i.e. the value of the exponent of this law, as a function of the volume fraction of powder will give a third value of the CSL.

In the first incremental method, the binder was first introduced into the mixer and then the powder was added in 2 % volume. The value of the mixing torque was measured as a function of time. After five to ten minutes of constant torque, the composite was considered a homogeneous mixture. The maximum powder loading was reached when the mixing torque was no longer stable, suggesting the appearance of inhomogeneities in the composite [36].

For the experimental methods (i.e. first and second ones), we introduce the optimal mixing time, denoted $\overline{t_{Fi}}$ for Fi (where i = 1 or 2) composite, which is the minimum time needed to obtain a homogeneous composite after the addition of powder counting from the appearance of the torque peak. In the permanent state following this transient instant, we also introduce the stabilized mixing torque, denoted $\overline{M_{Fi}}$ for Fi composite, as well as its fluctuation, denoted ΔM_{Fi}. A high value of $\overline{M_{Fi}}$ is related to a high shear rate viscosity and corresponds to a composite that is more suitable to the extrusion process.

The composites were finally mixed by the same twin-screw mixer and ground into fine homogeneous pellets, which are directly used in EAM 3D printers to manufacture mechanical parts.

2.4.2. Printing method of composites

The EAM process can be summarised in a few points: a computer-aided design (or CAD) model is converted into a tessellated geometry. A slicer used this file and configuration parameters (e.g. thickness of the deposited layer, nozzle and plate temperature, fill rate, and printing speed) are translated into Computer Numerical Control (or CNC) instructions for the machine [37]. FGF technology directly uses granules with low mechanical requirements. The Direct3D Pellet Extruder is suitable equipment for 3D printing with highly loaded magnetocaloric pellets. **Fig. 2** shows the extrusion process of the pellets which are pushed by a screw into the melting zone, where they are heated and melted. The molten composite was then extruded and deposited layer-by-layer onto a printing plate by moving the extrusion head to obtain different samples and parts in sections 4 and 5.

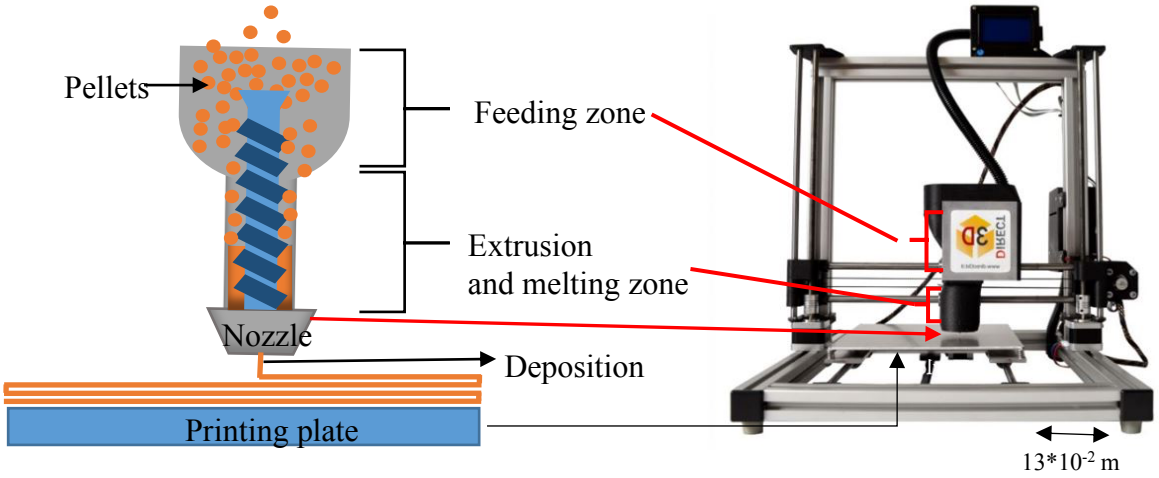

Fig. 2. Direct3D Pellet Extruder: Schematic description (on the left) and picture (on the right).

2.5. Method of characterising the mechanical behaviour

The characterisation of the mechanical behaviour of the composites was performed on printed specimens of conventional shape (115 mm long, 5 mm thick, 17 mm wide at the ends and 10 mm at the centre) with an aluminium reinforcement bonded to each of the ends. The mechanical stress consisted of applying about ten load-unload cycles (at a constant strain rate of 0.1 mm/min) with increasing amplitudes until the specimen broke. To quantify the viscoelasticity of the composite, stress relaxation was observed over a period of 30 s after each load and unload. From these characterisations, viscoelastic behaviour, apparent Young's modulus, damage, plastic deformation, yield strength and fracture values were derived at -20 °C, ambient (i.e. +20 °C) and +50 °C in

section 5.2. Due to progressive repeated mechanical loading, the stress-strain curve exhibits loops whose average slope gives the apparent Young's modulus while each return to zero stress gives the plastic strain.

These mechanical tests were performed using an Instron Electropuls® E10000 electrohydraulic tension-torsion machine equipped with a thermal chamber and an extensometer to determine the strain of the specimen. This machine can apply a maximum tensile-compression force of ±10 kN and a maximum torque of ±100 N·m up to 100 Hz and can control the temperature of the specimen between -70 °C and +350 °C.

3. Formulations of composites

In this section, one of the two available powder batches is selected from the Additive Manufacturing Suitability (or AMS) indicator and the critical solid powder loading (or CSL) level in the two formulated composites is determined by two different methods. Ultimately, the choice of the formulation of the composite that incorporates the highest volume fraction of powder is made for the rest of this work.

3.1. Characterisations of powders flow

The powders have been characterised by an FT4 Powder Rheometer. Powder flow behaviours are presented in **Fig. 3** and all physical properties obtained after post-treatment (see Appendix A for their expressions) are summarised in **Table 4**.

Presented in **Fig. 3**a, the dynamic downwards test shows the evolution of the flow energy measured for seven identical repeat tests on each powder followed by variable flow rate tests at reducing blade speeds. This flow energy *E* is more or less stable during these seven successive tests at 100 mm/s at a constant value of 1100 mJ for powder 1 and between 750 and 850 mJ for 2, then it increases when the speed of the blade decreases from 100 to 10 mm/s between the tests n° 8 to 11 as observed in [38]. The stabilised flow energy level (test n° 7) is the Basic Flowability Energy (or *BFE)* value and is a key flowability parameter because it reflects the resistances to forced flow. With a *BFE* value of 844 mJ versus 1110 mJ, powder 2 has a forced flow resistance 1.32 times smaller than powder 1, which gives powder 2 the most cohesion with the highest shear strength as presented in **Fig. 3**e [38]. Conversely, powder 1 has a better level of repeatability in this test with more stable rheology than powder 2, and, the Stability Index (or *SI*) is 0.99 for powder 1 versus 1.12 for powder 2. These small values of *SI* also indicate that both powders are not impacted by attrition or segregation [39]. The sensibility to blade speed or flow rate during these compaction tests is shown by tests n° 8 to 11 and is assessed by the Flow Rate Index (or *FRI*). The cohesive

powders require greater flow energy at lower rates because the entrained air can escape, leaving more resistant material to flow. Therefore, with an *FRI* value of 1.45 versus 1.22, powder 2 is more sensitive to flow rate and remains more cohesive than powder 1.

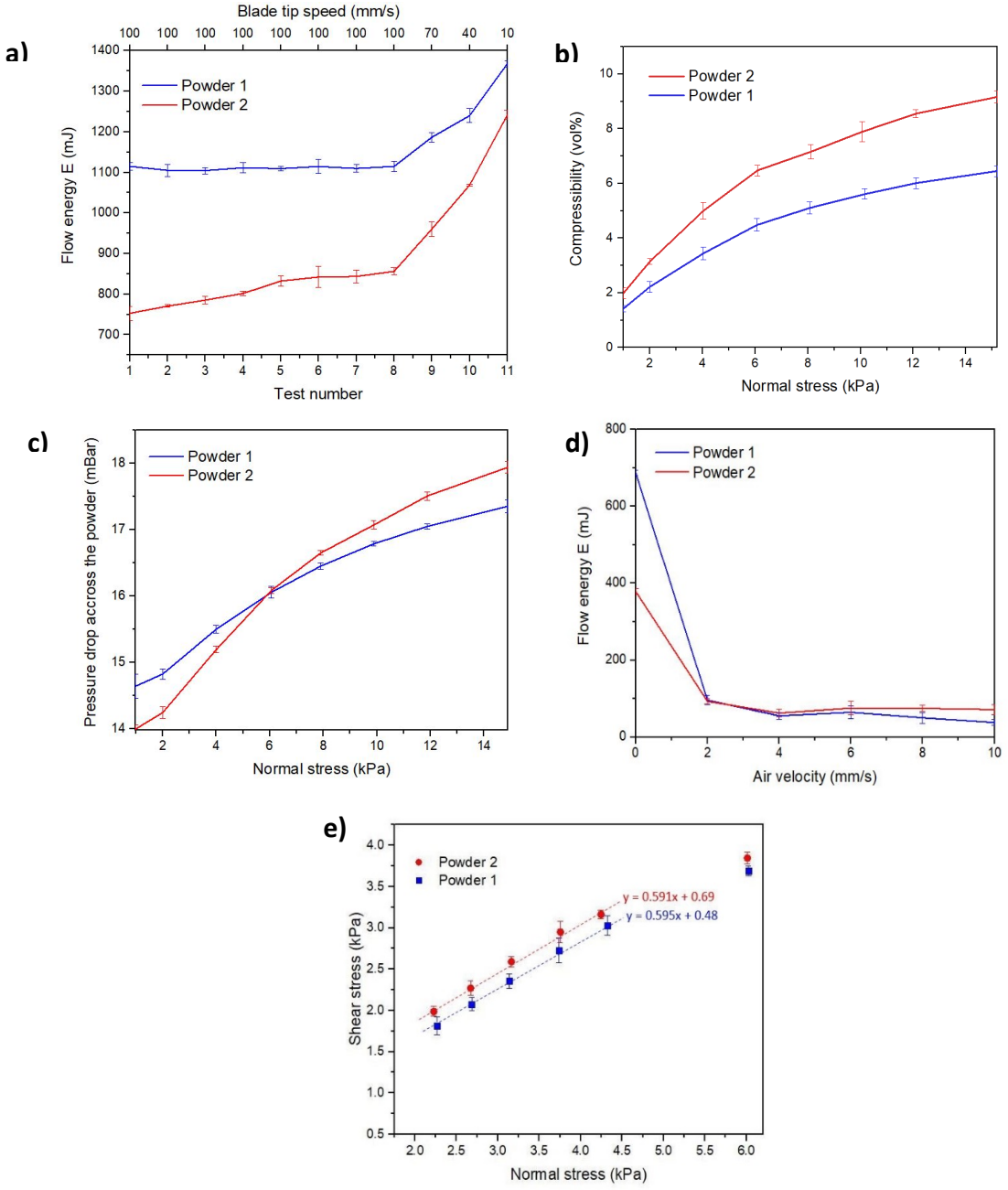

Fig. 3. a) Dynamic downwards test: Flow energy measurements at fixed and variable blade speeds. b) Compressibility test: Volume change versus applied normal stress. c) Permeability test: Pressure drop through powder bed at constant air velocity (2 mm/s) versus applied normal stress. d) Aeration test: Flow energy versus air velocity. e) Shear test: Shear stress versus normal stress of the sample consolidated and pre-sheared at 6 kPa normal stress.

The dynamic upwards test gives low and more or less identical values of the Specific Energy (or *SE*) for both powders (< 5 $mJ \cdot g^{-1}$), suggesting that they are overall weakly cohesive compared to other classical powders [40].

Presented in **Fig. 3**b, the compressibility test shows the evolution of the volume change as a function of the applied normal stress and reveals that both powders have a medium level of compressibility with a greater effect on powder 2. The value of the Compressibility Index (or *CI*) for a normal applied stress of 15 kPa is 9.15 % for powder 2 and 6.45 % for powder 1.

Presented in **Fig. 3**c, the permeability test shows the evolution of the pressure drop through the powder bed at constant air velocity (2 mm/s) as a function of the normal applied stress. Increasing the applied normal stress reduced the permeability of both powders and their Pressure drops (or *PD*) at a normal stress of 15 kPa is 17.4 mBar for powder 1 and 18 mBar for powder 2.

Presented in **Fig. 3**d, the aeration test shows the evolution of the flow energy as a function of air velocity. A rapid decrease (twice as fast for powder 1 as for powder 2) in the measured flow energy is observed for both powders with a value of minimum fluidisation velocity at 2 mm/s. The Aeration Energy (or *AE*) value at an air velocity of 10 mm/s is 37.8 mJ for powder 1 and 74.5 mJ for powder 2.

Presented in **Fig. 3**e, the shear test shows the shear stress as a function of the applied normal stress where the powder sample was pre-consolidated at 6 kPa. The cohesion coefficient c is obtained by performing a linear regression of the curve to identify the shear stress corresponding to zero normal stress. A value of c of 0.48 for powder 1 and 0.69 for powder 2 is obtained indicating a higher resistance to the flow of powder 2 during shearing.

Table 4

Powder flow properties of $La(Fe,Si)_{13}H$ powders defined in Appendix A and measured by FT4 rheometer analyses.

Powder characteristic	**Powder 1**	**Powder 2**
Bulk density ρ_c ($g \cdot cm^{-3}$)	3.31 ± 0.03	3.42 ± 0.03
Basic Flowability Energy *BFE* (mJ)	1110 ± 15	844 ± 15
Stability Index *SI* (1)	0.99 ± 0.05	1.12 ± 0.05
Flow Rate Index *FRI* (1)	1.22 ± 0.03	1.45 ± 0.03
Specific Energy *SE* ($mJ \cdot g^{-1}$)	4.36 ± 0.04	4.51 ± 0.04
Compressibility Index *CI* (%) (1)	6.45 ± 0.2	9.15 ± 0.2
Pressure Drop *PD* (mBar)	17.4 ± 0.1	18.0 ± 0.1
Aeration Energy *AE* (mJ)	37.8 ± 10	74.5 ± 10
Cohesion coefficient *c* (kPa)	0.48 ± 0.06	0.69 ± 0.06
Additive Manufacturing Suitability (or AMS) indicator (1)	0.65 ± 0.03	0.75 ± 0.03

From the set of flow properties identified and summarised in **Table 4**, the Additive Manufacturing Suitability (or AMS) indicator proposed by Brika et al. is calculated for both powders (using Eq. (8) recalled in the Appendix A). As powder 1 has the lowest AMS indicator, it is the most suitable for the development of the composite.

3.2. Determination of the CSL with continuously increasing powder loading method

The evolution of the mixing torque as a function of time for both formulations (F1 and F2 composites) is shown in **Fig. 4**a. The powder was mixed with binder 1 at the mixing temperature given in **Table 3** by intermittently adding a small amount of magnetocaloric powder. Each peak in **Fig. 4**a corresponds to the addition of powder in increments of 2 vol.%, its total concentration varying from 42 to 58 vol.% for powder 1 and from 40 to 54 vol.% for powder 2.

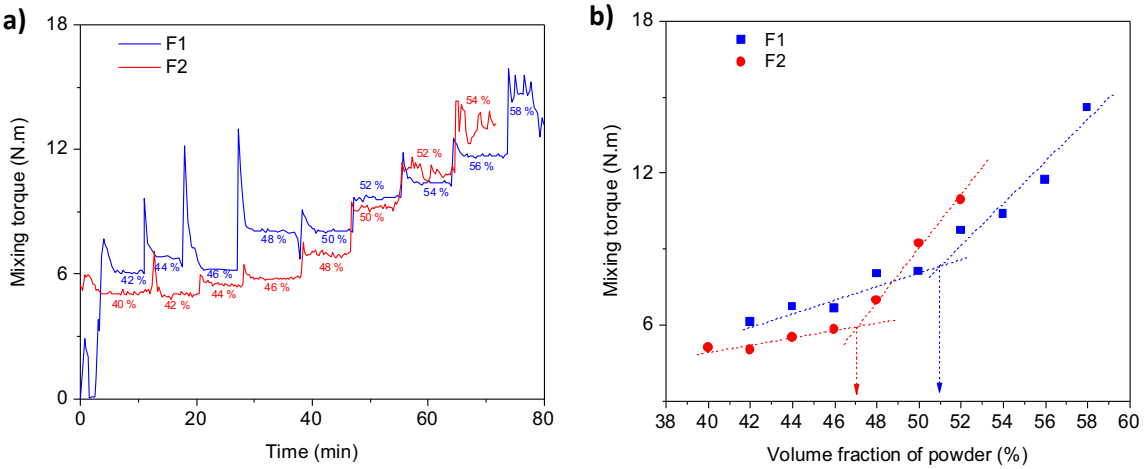

Fig. 4. Mixing of F1 and F2 composites: a) Mixing torque versus time with different volume fractions of powder, b) Stabilised mixing torque versus volume fraction of powder.

Fig. 4b shows the evolution of the stabilised mixing torque as a function of the volume fraction of powder. It reveals an evolution with two different slopes corresponding to the transition from a stable flow with a homogeneous mixture at a low volume fraction of powder to an unstable flow with an inhomogeneous mixture at a higher fraction. This stable/unstable transition defines the CSL which appears at 51% for the F1 composite and 47% for F2. The optimum volume fraction can be chosen as the CSL, but as with Ma et al [41], a value of 1 vol.% below the CSL is chosen in this work to ensure safe homogeneous mixing.

With this incremental method, the optimal volume fractions of powder φ_{op} obtained for both composites are summarised in **Table 5**.

Table 5

Critical and optimal volume fraction of powder, and, post-processing torque parameters measured in F1 and F2 composites.

Formulation	CSL ratio **(vol.%)**	φ_{op} **(vol.%)**	$\overline{t_{Fi}}$ **(min)**	$\overline{M_{Fi}}$ **(N·m)**	ΔM_{Fi} **(N·m)**
F1 composite	51	50	5.5	11	0.8
F2 composite	47	46	7.2	7	1.2

3.3. Determination of the CSL ratio with batch powder loading method

The batch powder loading method was used to fine-tune the optimal volume fraction determined by the previous continuous increment method. This method was applied within a narrower range of 50–52 vol.% for the F1 composite and 46–48 vol.% for F2. Different mixtures with a lower compositional gap of powder, i.e. 0.5 vol.%, were made and, as in the previous analysis, the final stabilised value of the mixing torque was analysed.

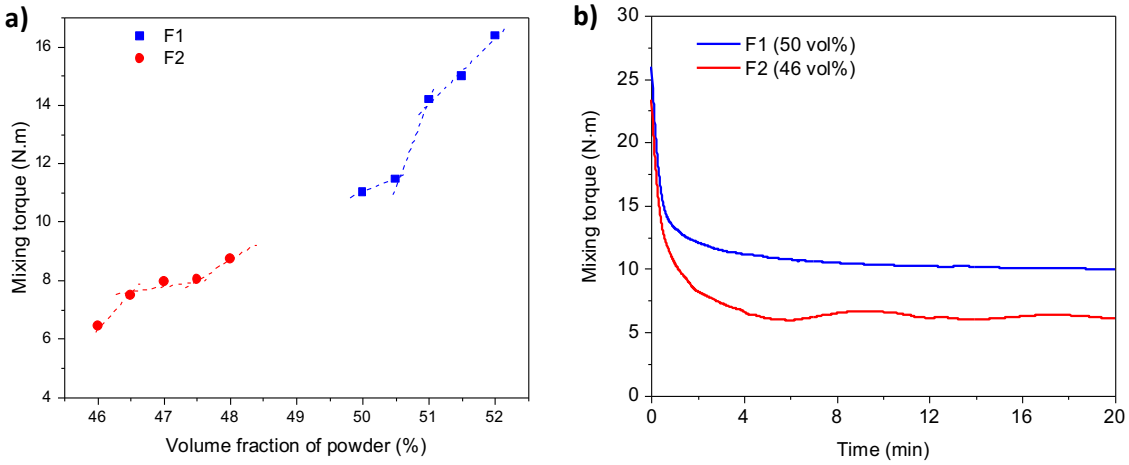

Fig. 5. Mixing torque of F1 and F2 composites a) versus volume fraction of powder, and, b) versus time by the batch powder loading method.

Fig. 5a shows the results for F1 and F2 composites for which their CSL ratio (i.e. the homogeneous/inhomogeneous transition) is identified as 50.5 and 46.5 vol.%, respectively. With this batch method, the volume fractions of 50 and 46 % were retained as the optimal powder loading for the F1 and F2 composites respectively.

Fig. 5b shows the mixing of composites F1 with 50 vol.% of powder and F2 with 46 vol.% leading to homogeneous mixtures with stabilised mixing torque values $\overline{M_{Fi}}$ at 11 ± 0.4 N·m after 5.5 min of mixing and 7 ± 0.6 N·m after 7.2 min, respectively. The F1 composite requires slightly less time

to become homogeneous than the F2. These high values of the mixing torque (about 10 N·m) are mainly due to the viscous behaviour of the polymer which is necessary for the extrusion process to keep the final shape of the manufactured part [21].

As a conclusion of this section III, a comparative analysis of the two methods used (i.e. the continuously increasing powder loading method, on the one hand, and the batch method, on the other) is summarised in **Table 6** with a presentation of their respective advantages and disadvantages. Finally, the formulation chosen is that of the most loaded composite corresponding to that of the F1 composite with a powder volume fraction of 50 % (A third method presented in Appendix B confirms this value of volume fraction). Furthermore, the stabilised value of the mixing torque of the F1 composite ensures that the binder-powder formulation is suitable for shaping by the FGF and FFF processes.

Table 6

Summary of the powder volume fraction study for F1 and F2 composites obtained by different mixing methods.

	Powder volume fraction (vol.%)		
Formulation		**Powder mixing method**	
		Continuously increasing loading	Batch loading
F1 composite	Range studied	42 – 58	50 – 52
	CSL ratio	51	50
F2 composite	Range studied	40 – 54	46 – 48
	CSL ratio	47	46
	Advantage of the method	Well-known and used by many authors	Sequential determination of load rates with different values
	Inconvenient of the method	Binder properties can be affected	-

4. Printing et shaping of the composite

In this section, a Rheological AMS (or RAMS) indicator is introduced to confirm the choice of the F1 composite as being the best suited for the elaboration and 3D printing processes. Details of 3D printing of small composite plates are also presented. Various homogeneity and porosity studies of these printed plates particularly by X-ray tomography, are then performed.

4.1. Ability of a composite formulation for high-loading and additive manufacturing

To help in choosing the best formulation among several, which is not always obvious, a rheological index adapted to additive manufacturing, called the Rheological AMS (or RAMS), is introduced

on the same basis as the AMS index reminded in the Appendix A. To maximise the optimal volume fraction of powder φ_{op} in a F_i composite and its stabilized mixing torque $\overline{M_{Fi}}$, and, to minimise its fluctuation of this torque ΔM_{Fi}, its RAMS indicator is defined as:

$$RAMS = \frac{1}{3}\left(\frac{1/\varphi_{op}}{(1/\varphi_{op})_{max}} + \frac{1/\overline{M_{Fi}}}{(1/\overline{M_{Fi}})_{max}} + \frac{\Delta M_{Fi}}{\Delta M_{Fi\_max}}\right) \quad (2)$$

From the values in **Table 5**, the calculation of this index for each of the two available formulations shows in **Table 7** that the smallest value of RAMS corresponding to the F1 formulation of the composite is the most suitable for the elaboration and printing processes. And in the rest of the study, only the F1 formulation of the composite will be used.

Table 7

Values of RAMS versus optimal volume fraction of powder and mixing parameters from **Table 5**.

Formulation	φ_{op} **(vol.%)**	$\overline{M_{Fi}}$ **(N·m)**	ΔM_{Fi} **(N·m)**	$RAMS$ **(1)**
F1 composite	50	11	0.8	0.72
F2 composite	46	7	1.2	1

Initially introduced by Weir [42], the mouldability index is also used to evaluate the rheological properties of composites during shaping by injection moulding [43]. The best injection conditions for the composite have the highest mouldability index [44]. For the 3D printing process by the FGF technique using screw extrusion at its head, the same index, denoted α, can be used:

$$\alpha = \frac{1}{\eta_0}\left|\frac{\partial\, log\, \eta}{\partial\, log\, \dot{\gamma}}\right| / \left(\frac{\partial\, log\, \eta}{\partial\, (1/T)}\right) = \frac{1}{\eta_0}\,\frac{1-n}{E_a/R} \quad (3)$$

where η_0, n, E_a and R denote the shear viscosity, power-law exponent, activation energy, and perfect gas constant, respectively.

This index calculated for the F1 composite at a temperature of 403 K and with a shear rate of 313 s^{-1} are given in **Table 8** with the values of η_0 , n, and E_a identified in Appendix B (see **Table 11**). This printing temperature and shear rate are determined in Appendix B for the printing nozzle and the composite used.

Table 8

Rheological characteristics and determined value of mouldability index for composite F1 at 403 K.

Temperature (K)	η_0 **(Pa·s)**	n **(1)**	E_a **(kJ·mol^{-1})**	α **(10^{-7} K^{-1}·Pa^{-1}·s^{-1})**
403	1103	0.26	23.26	2.39 ± 0.04

4.2. Geometry of small printed magnetocaloric plates

Fig. 6a shows the obtained geometry of the magnetocaloric small plate S1 and **Fig. 6**b the instruction path that the 3D printer follows. A skirt is necessary to ensure a stable flow so that the first layer

of the printed sample is filled. The sample surfaces depend on the printing path. The layers are crisscrossed at a +45°, then at a -45° angle in the XY plane.

Three samples were printed at a printing speed of 10^{-2} m/s. The shape of the printed surface and associated density showed no significant differences among these three specimens. The optimal ratio between the binder and volume fraction of powder allowed us to obtain non-brittle samples, unlike the magnetocaloric alloy in its bulk form [21].

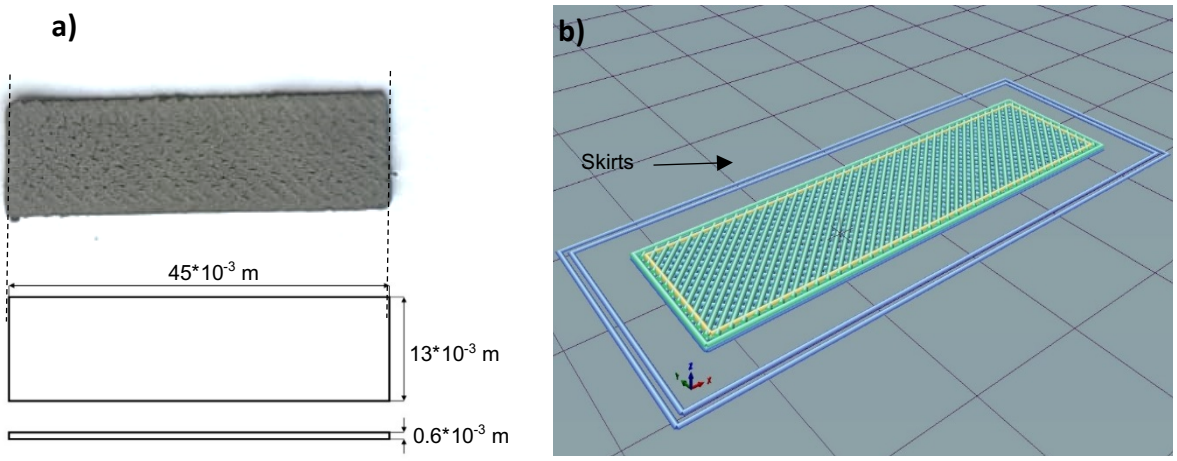

Fig. 6. Small printed plate S1: a) Plan of the small plate compared to the printed part, b) Image of the print head trajectories

4.3. Homogeneity and porosity of small printed plates

Fig. 7 shows SEM images of the free surface and a cross-section of a small printed composite plate. This free surface in **Fig. 7**a easily reveals the three superimposed printed layers with a surface roughness that is particular to the highly loaded composites. Except for a few large grains, the powder was perfectly covered by the binder, which means that the compatibility between the powder and the binder is adequate [45]. The cross-sectional back scattering SEM image obtained by cutting the small printed composite plate with a FEMTO-second laser is shown in **Fig. 7**b. This laser allows a sharp cut of the hard powder in its very soft matrix, as this figure clearly shown: on a black binder background, the white powder grains are very clear cutout and not torn out of the binder. It can also be seen that there are as many powder grains present as there is a binder (i.e. about 50 vol % as expected) and that they are homogeneously distributed in the composite.

The binder in a ferromagnetic powder-loaded composite is similar to porosity when it is non-ferromagnetic; it strongly attenuates the ferromagnetic behaviour due to the dilution phenomenon but also to the appearance of a higher demagnetising field than in the powder alone [46]. The

presence of voids (or empty cavities) in these printed composites, i.e. porosity, is also a cause of reduced volume properties but to a lesser extent while mechanical strength can be rapidly affected. Conversely, Rane et al. [11] have shown that the microscopic properties (i.e. porosity) and macroscopic one (i.e. geometry and density) of the samples improved with each step of the printing process. For all these reasons, the porosity of the printed composites is finally evaluated in the following.

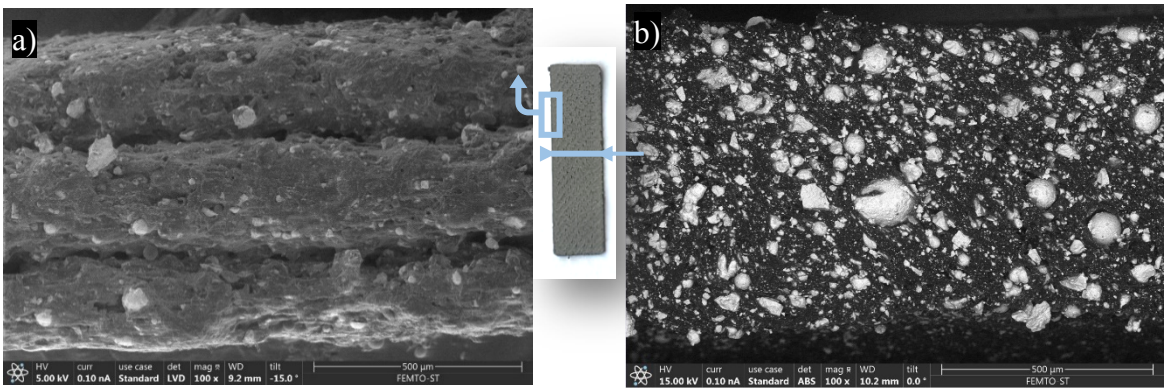

Fig. 7. In the middle, a top view of the small printed plate with the location of the Scanning Electron Microscopy observations of a) its free surface; b) a cross-section (a backscatter image).

X-ray tomographic analysis is used for estimating the volume of voids in printed parts. Here it is used to observe the pore distribution with a precision (or voxel size) of 5 μm^3. To obtain accurate results, a composite sample larger than the small plates, i.e. 10 × 10 × 3 mm^3, was made under the same conditions with more layers to be representative. **Fig. 8** exhibits the two cross-sections taken from this larger composite sample where the filaments pass through each of these sections at ± 45° to its normal (see bottom image). The pores were coloured according to their volume size. The tomographic observations show that the pores within this sample are quite small, numerous and homogenously distributed but also that no inter-filament porosity is identifiable, which would reveal the contour of the filaments. The pore sizes are principally lower than 2 10^{-3} mm^3 with few voids of 4 10^{-3} mm^3 volume and no structure related to the printed layer is observable. The tomographic analysis gives an indicative total porosity of 5.4 ± 1 % in the composite and therefore a porosity of 10.8 ± 2% in the binder (i.e. 5.4 ± 1% in 50 vol.% binder in the composite).

Finally, this porosity analysis shows that the numerous small pores are not associated with the printing process but, probably, with an energetic process over a long time such as mixing the powder with its binder. This analysis also shows that the printing process of the composite does not

eliminate this fine porosity although it does optimise the filling of the composite and its compactness.

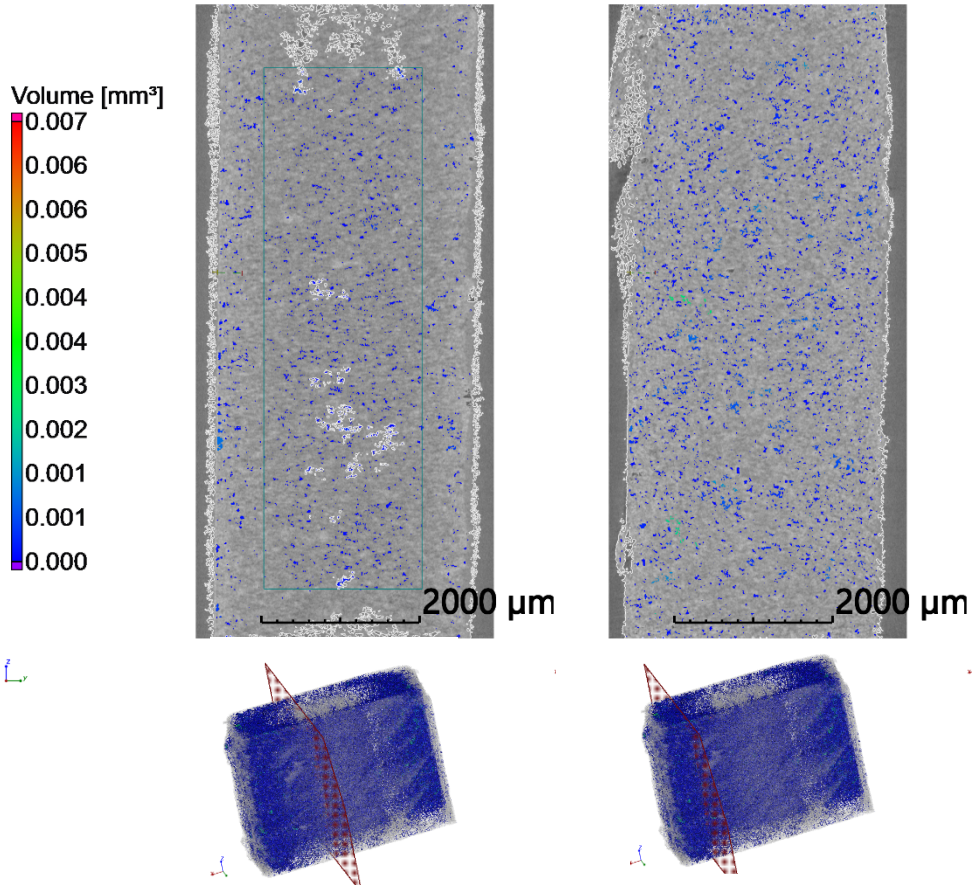

Fig. 8. X-ray tomographic analysis of two cross-sections of a larger composite and their localizations in the images below.

5. Macroscopic behaviours relevant to magnetocaloric applications

In this section, the characterization of the magnetocaloric properties is performed in order, on the one hand, to quantify them for the composite highly loaded with magnetocaloric powder and then, on the other hand, to verify that those of the powder have not been affected by the process for producing the composite and shaping it. Finally, a characterization of the mechanical properties of the final printed composite parts and a comparison with the same formulation of extruded parts are performed to know their respective mechanical limits to consider applications.

5.1. Magnetocaloric properties

The magnetocaloric effect (or MCE) in a material is characterised by its production or absorption of heat (or thermal energy) when it's subjected to a variation in magnetic field in the vicinity of its phase transition temperature, denoted T_{tr}. As mentioned above, the MCE of LaFeSi alloy in the form of powder or incorporated into a composite is closely dependent on its hydrogen content. A temperature higher than 453 K during the manufacturing or forming process of the composite could lead to its dehydrogenation and cause a shift of T_{tr} and an attenuation of the magnetocaloric effect. To verify a possible loss of hydrogen, Differential Scanning Calorimetry (or DSC) measurements were performed at the beginning of the process with the powder alone and at the end with the small printed plate of composite. The exploitation of these measurements allowed us to identify the phase transition properties, i.e. the transition temperature T_{tr}, the latent heat (or the enthalpy variation) ΔH_{tr} and the entropy change Δs.

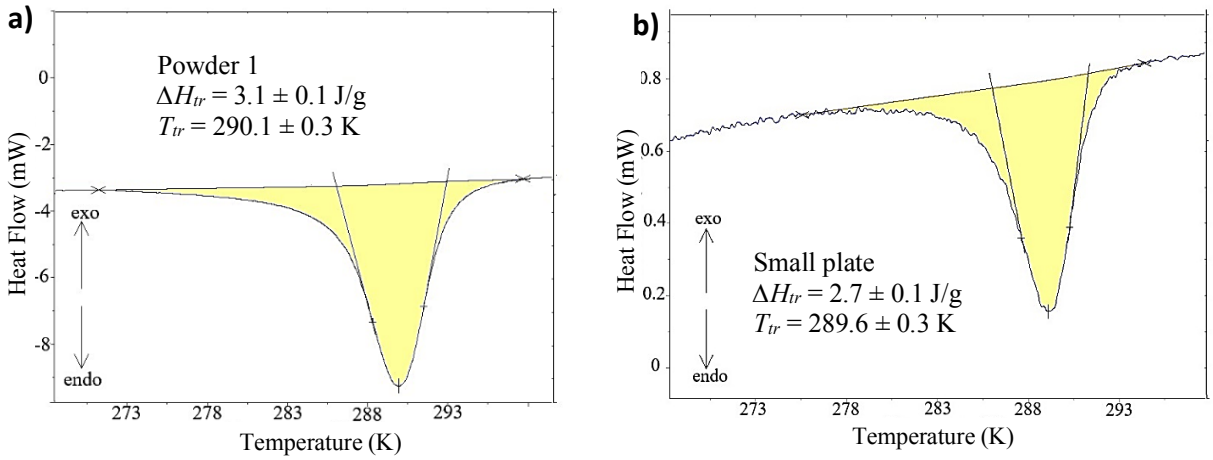

Fig. 9. DSC analysis of the phase transition: Identification of the latent heat ΔH_{tr} and the transition temperature T_{tr} of a) powder 1 and b) the small printed plate.

Fig. 9a and b show the endothermic peaks obtained by DSC of powder 1 and the small plate during their heating at a rate of 3 K/min. The minimum value of these peaks corresponds to the phase transition temperature T_{tr}. The latent heat of phase transition is determined by the area above these endothermic peaks and the corresponding entropy change is evaluated using the following equation proposed by Ito et al [47] such that

$$\Delta s = \frac{\Delta H_{tr}}{T_{tr}} \tag{4}$$

Table 9 gathers the identified values due to this phase transition. For each sample, there is no major difference in the transition temperature T_{tr} because it is very close to the supplier's reference

temperature of 290 ± 1 K. These DSC measurements also show that the phase transition starts at around 275 K and ends at around 295 K. Therefore, the spreading of the phase transition which is 20 K is not influenced, or even delayed, by the presence of the binder for this slow rate of heating. The values of the enthalpy variation of powder 1 and the small printed plate show a difference of 13 %. As enthalpy is an extensive thermodynamic quantity, it is therefore proportional to the mass (or volume) of the constituents of the sample under analysis. During the phase transition by heating, only the composite powder produces cold (or absorbs thermal energy by an endothermic reaction), while the binder absorbs a small amount of this heat depending on its heat capacity, its mass and the temperature increase needed to pass the transition. If this absorption is negligible, it is possible to compare these two results by relating the enthalpy variation of the small printed plate to the effective mass of powder in it. As the composite contains 50 % by volume of powder, i.e. 89 % by mass, the value of its enthalpy change corresponds to 89 % of that of the powder, i.e. 2759 ± 10^2 J/(kg of powder embedded in the composite) which is now slightly higher (by +2.18 %), but within the tolerance range, than the measured value of 2700 ± 10^2 J/kg. This small deviation can be explained by the heat absorption of the binder which was neglected, by a slightly lower powder concentration in the measured sample but also by the measurement uncertainties.

Table 9

Evaluation of the transition temperature T_{tr}, the enthalpy change ΔH_{tr} and the entropy change Δs of powder 1 and the small printed plate.

Sample	T_{tr} **(K)**	ΔH_{tr} **(J·kg^{-1})**	Δs **(J·K^{-1}·kg^{-1})**
Powder 1	290.10 ± 0.3	3.1 10^3 ± 10^2	10.68 ± 0.36
Small printed plate	289.60 ± 0.3	2.7 10^3 ± 10^2	9.32 ± 0.36

Finally, these DSC results ensure that the elaboration and shaping processes of the composite do not alter the magnetocaloric properties of the powder, especially its dehydrogenation, and, consequently, that we are indeed in the context of a so-called impression 4D which "preserves the properties".

5.2. Mechanical behaviours

5.2.1. Determination of the yield strength and fracture limits of the printed composite

The stress-strain cycles measured on the printed composite are shown in **Fig. 10** and illustrate the damageable viscoplastic non-linear response of the composite, i.e. with a viscous behaviour due to the polymer binder and a loss of the rigidity of the composite increasing with its level of stress [48]. The maximum deformation of the composite at room temperature (i.e. 20 °C) is about 4.6 %, i.e. about 5 times lower than that obtained with the unfilled polymeric binder. Conversely, its maximum

stress to rupture is about 2.2 MPa, i.e. 72 % greater than that of binder 1 alone which is 1.5 MPa. The powder within the composite acts as a mechanical stiffener for the binder (see, for example, [32, 49, 50]).

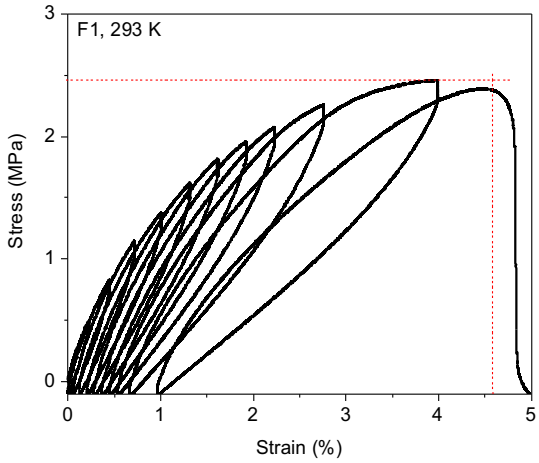

Fig. 10. Stress-strain response of printed composite subjected to repeated progressive mechanical loading and unloading at room temperature until fracture.

In **Fig. 11**, the characterisation with repeated progressive mechanical loading and unloading allows determining the evolution of the plastic strain ε_p accumulated in the specimen as well as its damage as a function of the maximum stress, i.e. the maximum level of stress that was seen by the composite [51]. In this figure, the damage appears as the decay of Apparent Young's modulus E_{app} as a function of the maximum stress.

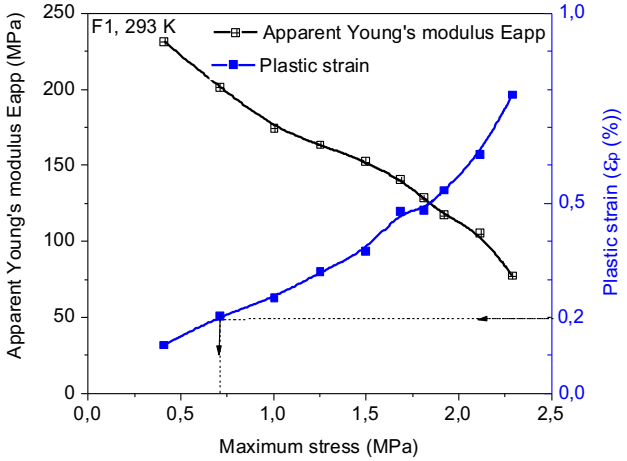

Fig. 11. Changes in Apparent Young's modulus E_{app} and plastic strain ε_p as a function of maximum stress at room temperature of the printed composite. Estimation of its yield strength at 0.2% plastic strain.

For a plastic strain level set at 0.2 %, the yield strength is identified in **Fig. 11** as approximately 0.7 MPa for the printed composite at room temperature, whereas it is 0.2 MPa for the binder alone. These yield strength values are very low compared to the values reported in the literature for polymers and composites used as a structural material, which is an obstacle for an industrial application particularly to resist the pressure of a heat transfer fluid or, more simply, assembly stresses and FFF printing [52, 53]. However, at -20 °C or 253 K (i.e. a difference of 72 °C or K from the lowest melting temperature of the constituents which is EVA), its yield strength increases to 5 MPa which begins to be a reasonable value to consider the use of this formulation of the composite respecting the non-dehydrogenation of the LaFeSi powder for magnetocaloric applications.

5.2.2. Comparison of the mechanical properties of printed composite with extruded strips

Most of the results in the literature show that compression moulded [54, 55] or injection moulded [56, 57] parts have better mechanical properties than printed parts. The reason for this difference is the defects caused by the printing process or, more generally, by the presence of voids and porosity, as shown by H. L. Tekinalp et al [54]. This difference can be reduced by decreasing the presence of voids and porosities or, as was done in this study, by optimising the printing parameters. However, due to the significant effect of temperature on the mechanical properties, this comparison becomes less obvious, as we shall see.

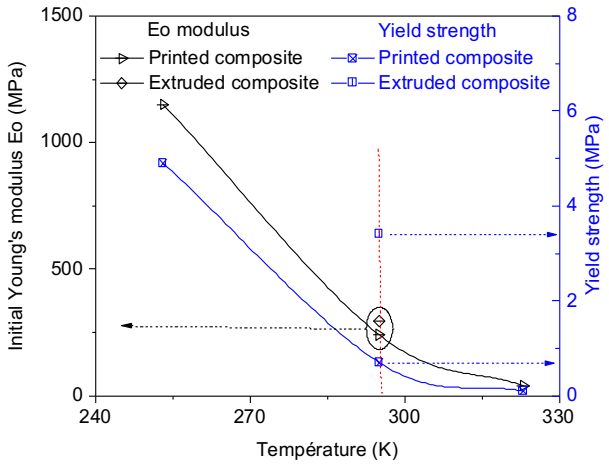

Fig. 12. Evolutions of the initial Young's modulus E_0 and yield strength as a function of the temperature of the printed composite and the extruded strip (magnetocaloric).

To compare these mechanical properties of the printed composite with those of the same composite (same composition, same formulation and same powder with the same filler content) shaped conventionally by extrusion, the magnetocaloric strips extruded in the framework of J. Lanzarini's thesis work were characterized using the same protocol. The value of the ultimate tensile stress at room temperature was found to be about 5.3 MPa, i.e. 2.4 times greater than that of the printed component with an almost identical ultimate strain. **Fig. 12** shows the evolution of the yield strength and initial Young's modulus of each of the printed and extruded composites as a function of their temperature. It also shows that the yield strength and initial Young's modulus evolve in the same way, i.e. non-linear way with temperature. Finally, this figure shows that the same level of yield strength is obtained when the printed composite is used at a temperature about 30 °C lower than that of the same extruded composite. It also shows that at room temperature the yield strength is about 5 times greater in favour of the extruded composite (i.e. 3.4 MPa versus 0.7 MPa) while the initial Young's moduli are equivalent to about 240 ± 10 MPa, which is probably due to the fine porosity of about 10.8 ± 2 % (i.e. 5.4 ± 1 % overall porosity in 50 vol.% binder in the composite) present in the binder of the printed composite whereas it is about 4% in the binder of the extruded composite.

6. Conclusion

This work seeks to develop magnetocaloric plates by an additive manufacturing process from highly loaded fused composite granules of $La(Fe,Si)_{13}H$ magnetocaloric powders. The incorporation of as much powder as possible in a binder based on LDPE and EVA was studied by three different methods giving an optimum volume fraction of 50% powder. Three selection criteria were defined to help choose the best powder (AMS indicator), composite formulation (RAMS indicator) and printing process parameters (mouldability index). These three criteria are both independent and essential for the optimisation of the overall printing process for high powder composites. The composite pellets were then used in a Direct3D pellet extruder. A study of the homogeneity, porosity and hole mapping by X-ray tomography of printed composite samples reveals a homogeneous distribution of the powder with an overall porosity of about 5.4 ± 1 % in the composite, or about 10.8 ± 2% in the binder, present as pores sizes of less than 2.10^{-3} mm^3 and with some voids of 4.10^{-3} mm^3. This fine and homogeneous porosity seems to originate from the mixing process of the powder with its binder and is not removed when the composite pellets are extruded into the printhead. To ensure the viability of the elaboration and shaping processes for magnetocaloric applications, the conservation of the phase transition temperature was verified by

DSC analysis. This study also shows that due to the high mass fraction of 89% of $La(Fe,Si)_{13}H$ magnetocaloric powder, the entropy variation of the loaded composite with 9.3 $J \cdot K^{-1} \cdot kg^{-1}$ is only very slightly lower than that of the powder alone which is 10.7 $J \cdot K^{-1} \cdot kg^{-1}$, i.e. 13 % lower, placing this work in the context of 4D printing. Tensile tests on samples of the printed composite were carried out to determine their mechanical properties and quantify the damage. This composite exhibits a damageable viscoplastic behaviour with a small elastic range; The study of the evolution of plastic deformation as a function of the maximum stress experienced by this printed composite identified its yield strength at room temperature at 0.7 MPa, which is too low to consider its use as a structural material in an industrial application and in particular for FFF printing. However, at -20 °C with a deviation of 72°C from the lowest melting temperature of the constituents, its yield strength increases to 5 MPa, which starts to be a reasonable value for magnetocaloric applications with LaFeSi powder. Finally, a comparison with extruded strips of the composite of the same formulation shows that its yield strength is about 5 times higher while initial Young's moduli are the same, which is probably due to the 2-fold higher porosity in the binder of the printed composite compared to that of the extruded composite (10.8 ± 2% versus 4%). This last result gives the scope for improvement of the overall printing process developed in this study.

Glossary

AMS	Additive Manufacturing Suitability
ASTM	American Society for Testing Material
CAD	Computer-Aided Design
CNC	Computer Numerical Control
CSL	Critical Solid Loading
DSC	Differential Scanning Calorimetry
EAM	Extrusion-based Additive Manufacturing
EVA	Ethylene Vinyl Acetate
FFF	Fused-Filament Fabrication
FGF	Fused Granular Fabrication
FT4	Freeman Technology powder rheometer
LDPE	Low Density PolyEthylene
MCE	MagnetoCaloric Effect
PLA	PolyLactic Acid
RAMS	Rheological Additive Manufacturing Suitability
SA	Stearic Acid
SEM	Scanning Electron Microscopy
a	Newtonian regime transition width
AE	Aeration Energy
B	Shear viscosity at a fixed shear rate and volume fraction of powder
BFE	Basic Flowability Energy
c	Cohesion coefficient
CI	Compressibility Index
d_X	Particle size at X %
E_a	Activation energy
f	Printing speed
FRI	Flow Rate Index
h	Height of the deposited filament
ΔH_{tr}	Latent heat (or Enthalpy change)
K	Flow consistency index
K_0	Constant
m	Powder exponent of the effect of the powder volume fraction
$\overline{M}_{Fi}$	Stabilized mixing torque
ΔM_{Fi}	Fluctuation mixing torque
n	Power-law exponent
PD	Pression Drop
R	Gas constant
SE	Specific Energy
SI	Stability Index
S_w	Slope of particle size distribution
Δs	Change of entropy
$\bar{t}$	Optimum mixing time
T	Temperature
T_f	Melting temperature
T_{tr}	Transition temperature
$\bar{V}$	Average inlet velocity
x_{pi}	Weight fraction of the component pi
α	Mouldability index
$\dot{\gamma}$	Shear rate

φ	Volume fraction of powder
φ_{op}	Optimal volume fraction of powder
η	Shear viscosity
η_0	Shear viscosity at reference temperature and without shear rate
$\Delta\eta$	Shear viscosity difference between model and experiment
λ	Relaxation time
ρ_c	Bulk density

Bibliography

[1] N.A. Mezaal, K.V. Osintsev, T.B. Zhirgalova, Review of magnetic refrigeration system as alternative to conventional refrigeration system, IOP Conf. Ser.: Earth Environ. Sci. 87 (2017) 032024. https://doi.org/10.1088/1755-1315/87/3/032024.

[2] V. Franco, J.S. Blázquez, J.J. Ipus, J.Y. Law, L.M. Moreno-Ramírez, A. Conde, Magnetocaloric effect: From materials research to refrigeration devices, Progress in Materials Science. 93 (2018) 112–232. https://doi.org/10.1016/j.pmatsci.2017.10.005.

[3] E. Brück, O. Tegus, L. Zhang, X.W. Li, F.R. de Boer, K.H.J. Buschow, Magnetic refrigeration near room temperature with Fe_2P-based compounds, Journal of Alloys and Compounds. 383 (2004) 32–36. https://doi.org/10.1016/j.jallcom.2004.04.042.

[4] M. Balli, S. Jandl, P. Fournier, A. Kedous-Lebouc, Advanced materials for magnetic cooling: Fundamentals and practical aspects, Applied Physics Reviews. 4 (2017) 021305. https://doi.org/10.1063/1.4983612.

[5] M. Phejar, V. Paul-Boncour, L. Bessais, Structural and magnetic properties of magnetocaloric $LaFe_{13-x}Si_x$ compounds synthesized by high energy ball-milling, Intermetallics. 18 (2010) 2301–2307. https://doi.org/10.1016/j.intermet.2010.07.022.

[6] H.E. Sabzi, S. Maeng, X. Liang, M. Simonelli, N.T. Aboulkhair, P.E.J. Rivera-Díaz-del-Castillo, Controlling crack formation and porosity in laser powder bed fusion: Alloy design and process optimisation, Additive Manufacturing. 34 (2020) 101360. https://doi.org/10.1016/j.addma.2020.101360.

[7] N. Yang, C. You, N. Tian, Y. Zhang, H. Leng, J. He, Simultaneous plate forming and hydriding of $La(Fe, Si)_{13}$ magnetocaloric powders, Journal of Magnetism and Magnetic Materials. 451 (2018) 47–50. https://doi.org/10.1016/j.jmmm.2017.10.123.

[8] I. Flores Ituarte, O. Wiikinkoski, A. Jansson, Additive Manufacturing of Polypropylene: A Screening Design of Experiment Using Laser-Based Powder Bed Fusion, Polymers. 10 (2018) 1293. https://doi.org/10.3390/polym10121293.

[9] K. Rane, M. Strano, A comprehensive review of extrusion-based additive manufacturing processes for rapid production of metallic and ceramic parts, Adv. Manuf. 7 (2019) 155–173. https://doi.org/10.1007/s40436-019-00253-6.

[10] K. Elkins, H.D. Nordby, C. Janak, R.W.G. Iv, J.H. Bøhn, D.G. Baird, Soft Elastomers for Fused Deposition Modeling, in: 1997. https://doi.org/10.15781/T2833NJ55.

[11] K. Rane, S. Petrò, M. Strano, Evolution of porosity and geometrical quality through the ceramic extrusion additive manufacturing process stages, Additive Manufacturing. 32 (2020) 101038. https://doi.org/10.1016/j.addma.2020.101038.

[12] J. Jiang, J. Lou, G. Hu, Effect of support on printed properties in fused deposition modelling processes, Virtual and Physical Prototyping. 14 (2019) 308–315. https://doi.org/10.1080/17452759.2019.1568835.

[13] J. Jiang, X. Xu, J. Stringer, Optimization of process planning for reducing material waste in extrusion based additive manufacturing, Robotics and Computer-Integrated Manufacturing. 59 (2019) 317–325. https://doi.org/10.1016/j.rcim.2019.05.007.

[14] E.M. Palmero, D. Casaleiz, J. de Vicente, B. Skårman, H. Vidarsson, P.-O. Larsson, A. Bollero, Effect of particle size distribution on obtaining novel MnAlC-based permanent magnet composites and flexible filaments for 3D-printing, Additive Manufacturing. 33 (2020) 101179. https://doi.org/10.1016/j.addma.2020.101179.

[15] T.M. Oyinloye, W.B. Yoon, Stability of 3D printing using a mixture of pea protein and alginate: Precision and application of additive layer manufacturing simulation approach for stress distribution, Journal of Food Engineering. 288 (2021) 110127. https://doi.org/10.1016/j.jfoodeng.2020.110127.

[16] L. Chaunier, S. Guessasma, S. Belhabib, G. Della Valle, D. Lourdin, E. Leroy, Material extrusion of plant biopolymers: Opportunities & challenges for 3D printing, Additive

Manufacturing. 21 (2018) 220–233. https://doi.org/10.1016/j.addma.2018.03.016.
[17] C.G. Schirmeister, T. Hees, E.H. Licht, R. Mülhaupt, 3D printing of high density polyethylene by fused filament fabrication, Additive Manufacturing. 28 (2019) 152–159. https://doi.org/10.1016/j.addma.2019.05.003.
[18] A. Royer, T. Barriere, J.C. Gelin, The degradation of poly(ethylene glycol) in an Inconel 718 feedstock in the metal injection moulding process, Powder Technology. 284 (2015) 467–474. https://doi.org/10.1016/j.powtec.2015.07.032.
[19] E. Hnatkova, B. Hausnerova, P. Filip, Evaluation of powder loading and flow properties of Al_2O_3 ceramic injection molding feedstocks treated with stearic acid, Ceramics International. 45 (2019) 20084–20090. https://doi.org/10.1016/j.ceramint.2019.06.273.
[20] L. Gorjan, L. Reiff, A. Liersch, F. Clemens, Ethylene vinyl acetate as a binder for additive manufacturing of tricalcium phosphate bio-ceramics, Ceramics International. 44 (2018) 15817–15823. https://doi.org/10.1016/j.ceramint.2018.05.260.
[21] J. Lanzarini, M. Sahli, T. Barriere, A. Dubrez, C. Mayer, M. Pierronnet, P. Vikner, Experimental investigations on the process of forming functional microstructured blades from highly filled thermoplastic composites prepared with La(Fe, Si)$_{13}$ alloys, Journal of Materials Processing Technology. 273 (2019) 116244. https://doi.org/10.1016/j.jmatprotec.2019.05.025.
[22] R.M. German, A. Bose, Injection Moulding of Metals and Ceramics, Metals Powder Industries Federation, Princeton, New Jersey, USA, 1997. https://www.techstreet.com/mpif/searches/35720771.
[23] C. Mayer, A. Dubrez, M. Pierronnet, P. Vikner, Towards the large scale production of $(La_{1-z}Ce_z)(Fe_{1-x-y}Mn_ySi_x)_{13}H_n$ products for room temperature refrigeration: Towards the large scale production of $(La_{1-z}Ce_z)(Fe_{1-x-y}Mn_ySi_x)_{13}H_n$ products for room temperature refrigeration, Phys. Status Solidi C. 11 (2014) 1059–1063. https://doi.org/10.1002/pssc.201300650.
[24] C. Kukla, J. Gonzalez-Gutierrez, I. Duretek, S. Schuschnigg, C. Holzer, Effect of particle size on the properties of highly-filled polymers for fused filament fabrication, in: Lyon, France, 2017: p. 190006. https://doi.org/10.1063/1.5016795.
[25] C. Dimitri, S. Mohamed, B. Thierry, G. Jean-Claude, Influence of particle-size distribution and temperature on the rheological properties of highly concentrated Inconel feedstock alloy 718, Powder Technology. 322 (2017) 273–289. https://doi.org/10.1016/j.powtec.2017.08.049.
[26] B. Hausnerova, B.N. Mukund, D. Sanetrnik, Rheological properties of gas and water atomized 17-4PH stainless steel MIM feedstocks: Effect of powder shape and size, Powder Technology. 312 (2017) 152–158. https://doi.org/10.1016/j.powtec.2017.02.023.
[27] J.H. Tan, W.L.E. Wong, K.W. Dalgarno, An overview of powder granulometry on feedstock and part performance in the selective laser melting process, Additive Manufacturing. 18 (2017) 228–255. https://doi.org/10.1016/j.addma.2017.10.011.
[28] J. Lanzarini, T. Barriere, M. Sahli, J.C. Gelin, A. Dubrez, C. Mayer, M. Pierronnet, P. Vikner, Thermoplastic filled with magnetocaloric powder, Materials & Design. 87 (2015) 1022–1029. https://doi.org/10.1016/j.matdes.2015.08.057.
[29] C. Karatas, A. Kocer, H.I. Ünal, S. Saritas, Rheological properties of feedstocks prepared with steatite powder and polyethylene-based thermoplastic binders, Journal of Materials Processing Technology. 152 (2004) 77–83. https://doi.org/10.1016/j.jmatprotec.2004.03.009.
[30] M. Khakbiz, A. Simchi, R. Bagheri, Analysis of the rheological behavior and stability of 316L stainless steel–TiC powder injection molding feedstock, Materials Science and Engineering: A. 407 (2005) 105–113. https://doi.org/10.1016/j.msea.2005.06.057.
[31] J. Lanzarini, T. Barriere, M. Sahli, J.C. Gelin, A. Dubrez, C. Mayer, M. Pierronnet, P. Vikner, Thermoplastic filled with magnetocaloric powder, Materials & Design. 87 (2015)

1022–1029. https://doi.org/10.1016/j.matdes.2015.08.057.
[32] J. Lanzarini, Elaboration et caractérisation thermo-physique de micro-composants fonctionnels à base de poudres magnétocaloriques, PhD thesis, Besançon, 2016. https://www.theses.fr/2016BESA2053.
[33] J. Lanzarini, M. Sahli, T. Barriere, A. Dubrez, C. Mayer, M. Pierronnet, P. Vikner, Experimental investigations on the process of forming functional microstructured blades from highly filled thermoplastic composites prepared with La(Fe, Si)$_{13}$ alloys, Journal of Materials Processing Technology. 273 (2019) 116244. https://doi.org/10.1016/j.jmatprotec.2019.05.025.
[34] M.M.H. Kuroda, C.E. Scott, Blade geometry effects on initial dispersion of chopped glass fibers, Polymer Composites. 23 (2002) 828–838. https://doi.org/10.1002/pc.10481.
[35] J.R. Campanelli, C. Gurer, T.L. Rose, J.E. Varner, Dispersion, temperature and torque models for an internal mixer, Polymer Engineering & Science. 44 (2004) 1247–1257. https://doi.org/10.1002/pen.20120.
[36] N. Zainon, M.A. Omar, R. Sauti, M. Marzuki, Elucidating the influences of torque and energy in determining optimal loading, Materials Today: Proceedings. 16 (2019) 2144–2152. https://doi.org/10.1016/j.matpr.2019.06.104.
[37] J.W. Arblaster, Selected Electrical Resistivity Values for the Platinum Group of Metals Part I: Palladium and Platinum, Johnson Matthey Technol Rev. 59 (2015) 174–181. https://doi.org/10.1595/205651315X688091.
[38] R. Freeman, Measuring the flow properties of consolidated, conditioned and aerated powders — A comparative study using a powder rheometer and a rotational shear cell, Powder Technology. 174 (2007) 25–33. https://doi.org/10.1016/j.powtec.2006.10.016.
[39] B. Chen, R. Davies, Y. Liu, N. Yi, D. Qiang, Y. Zhu, O. Ghita, Laser sintering of graphene nanoplatelets encapsulated polyamide powders, Additive Manufacturing. 35 (2020) 101363. https://doi.org/10.1016/j.addma.2020.101363.
[40] R. Groarke, C. Danilenkoff, S. Karam, E. McCarthy, B. Michel, A. Mussatto, J. Sloane, A. O' Neill, R. Raghavendra, D. Brabazon, 316L Stainless Steel Powders for Additive Manufacturing: Relationships of Powder Rheology, Size, Size Distribution to Part Properties, Materials. 13 (2020) 5537. https://doi.org/10.3390/ma13235537.
[41] H. Ma, S. Li, Z. Jin, Y. Tian, F. Ren, Z. Zhou, W. Xu, Effect of 17-4PH stainless steel powders interaction on feedstocks, Powder Technology. 372 (2020) 204–211. https://doi.org/10.1016/j.powtec.2020.05.106.
[42] F.E. Weir, Moldability of plastics based on melt rheology. Part 1—theoretical development, Polymer Engineering & Science. 3 (1963) 32–36. https://doi.org/10.1002/pen.760030108.
[43] G. Aggarwal, S.J. Park, I. Smid, Development of niobium powder injection molding: Part I. Feedstock and injection molding, International Journal of Refractory Metals and Hard Materials. 24 (2006) 253–262. https://doi.org/10.1016/j.ijrmhm.2005.06.003.
[44] H. Zakaria, N. Muhamad, A.B. Sulong, M.H.I. Ibrahim, F. Foudzi, Moldability characteristics of 3 mol% yttria stabilized zirconia feedstock for micro-powder injection molding process, Sains Malaysiana. 43 (2014) 129–136.
[45] J.M. Park, J.S. Han, J.W. Oh, S.J. Park, Study on Rheological Behavior and Mechanical Properties of PMN–PZT Ceramic Feedstock, Met. Mater. Int. (2019). https://doi.org/10.1007/s12540-019-00455-4.
[46] L. Li, K. Jones, B. Sales, J.L. Pries, I.C. Nlebedim, K. Jin, H. Bei, B.K. Post, M.S. Kesler, O. Rios, V. Kunc, R. Fredette, J. Ormerod, A. Williams, T.A. Lograsso, M.P. Paranthaman, Fabrication of highly dense isotropic Nd-Fe-B nylon bonded magnets via extrusion-based additive manufacturing, Additive Manufacturing. 21 (2018) 495–500. https://doi.org/10.1016/j.addma.2018.04.001.
[47] W. Ito, Y. Imano, R. Kainuma, Y. Sutou, K. Oikawa, K. Ishida, Martensitic and Magnetic Transformation Behaviors in Heusler-Type NiMnIn and NiCoMnIn Metamagnetic Shape

Memory Alloys, Metall and Mat Trans A. 38 (2007) 759–766. https://doi.org/10.1007/s11661-007-9094-9.
[48] H. Nouri, Modélisation et identification de lois de comportement avec endommagement en fatigue polycyclique de matériaux composite a matrice thermoplastique, PhD thesis, Arts et Métiers ParisTech, 2009. https://pastel.archives-ouvertes.fr/pastel-00005669.
[49] D. Nötzel, R. Eickhoff, T. Hanemann, Fused Filament Fabrication of Small Ceramic Components, Materials. 11 (2018) 1463. https://doi.org/10.3390/ma11081463.
[50] S. Bakrani Balani, F. Chabert, V. Nassiet, A. Cantarel, Influence of printing parameters on the stability of deposited beads in fused filament fabrication of poly(lactic) acid, Additive Manufacturing. 25 (2019) 112–121. https://doi.org/10.1016/j.addma.2018.10.012.
[51] P. Ladeveze, E. LeDantec, Damage modelling of the elementary ply for laminated composites, Composites Science and Technology. 43 (1992) 257–267. https://doi.org/10.1016/0266-3538(92)90097-M.
[52] C. G'Sell, Plasticité et endommagement des polymères structuraux, Actualité chimique. (2002) 40–43.
[53] G.D. Goh, Y.L. Yap, H.K.J. Tan, S.L. Sing, G.L. Goh, W.Y. Yeong, Process–Structure–Properties in Polymer Additive Manufacturing via Material Extrusion: A Review, Critical Reviews in Solid State and Materials Sciences. 45 (2020) 113–133. https://doi.org/10.1080/10408436.2018.1549977.
[54] H.L. Tekinalp, V. Kunc, G.M. Velez-Garcia, C.E. Duty, L.J. Love, A.K. Naskar, C.A. Blue, S. Ozcan, Highly oriented carbon fiber–polymer composites via additive manufacturing, Composites Science and Technology. 105 (2014) 144–150. https://doi.org/10.1016/j.compscitech.2014.10.009.
[55] O.S. Carneiro, A.F. Silva, R. Gomes, Fused deposition modeling with polypropylene, Materials & Design. 83 (2015) 768–776. https://doi.org/10.1016/j.matdes.2015.06.053.
[56] E. Kim, Y.-J. Shin, S.-H. Ahn, The effects of moisture and temperature on the mechanical properties of additive manufacturing components: fused deposition modeling, Rapid Prototyping Journal. 22 (2016) 887–894. https://doi.org/10.1108/RPJ-08-2015-0095.
[57] C. Hérard, Les effets de la température lors de la fabrication additive par FDM de composites thermoplastiques renforcés et leurs propriétés mécaniques, masters, École Polytechnique de Montréal, 2017. https://publications.polymtl.ca/2681/.
[58] J.M.V. Millán, Fluidization of Fine Powders: Cohesive versus Dynamical Aggregation, Springer Netherlands, 2013. https://doi.org/10.1007/978-94-007-5587-1.
[59] Z. Yan, S.K. Wilkinson, E.H. Stitt, M. Marigo, Investigating mixing and segregation using discrete element modelling (DEM) in the Freeman FT4 rheometer, International Journal of Pharmaceutics. 513 (2016) 38–48. https://doi.org/10.1016/j.ijpharm.2016.08.065.
[60] R. Freeman, Measuring the flow properties of consolidated, conditioned and aerated powders — A comparative study using a powder rheometer and a rotational shear cell, Powder Technology. 174 (2007) 25–33. https://doi.org/10.1016/j.powtec.2006.10.016.
[61] G. Forte, P.J. Clark, Z. Yan, E.H. Stitt, M. Marigo, Using a Freeman FT4 rheometer and Electrical Capacitance Tomography to assess powder blending, Powder Technology. 337 (2018) 25–35. https://doi.org/10.1016/j.powtec.2017.12.020.
[62] R. Freeman, X. Fu, Characterisation of powder bulk, dynamic flow and shear properties in relation to die filling, Powder Metallurgy. 51 (2008) 196–201. https://doi.org/10.1179/174329008X324115.
[63] L.P. Lefebvre, J. Whiting, B. Nijikovsky, S.E. Brika, H. Fayazfar, O. Lyckfeldt, Assessing the robustness of powder rheology and permeability measurements, Additive Manufacturing. 35 (2020) 101203. https://doi.org/10.1016/j.addma.2020.101203.
[64] H. Lu, J. Cao, X. Guo, X. Gong, C. Luo, Evaluation of powder tensile strength by compression, shear and fluidization modules of the powder rheometer, Chemical Engineering Research and Design. 160 (2020) 1–10.

https://doi.org/10.1016/j.cherd.2020.05.026.
[65] H. Louati, X. Bednarek, S. Martin, A. Ndiaye, O. Bonnefoy, Qualitative and quantitative DEM analysis of cohesive granular material behaviour in FT4 shear tester, Chemical Engineering Research and Design. 148 (2019) 155–163. https://doi.org/10.1016/j.cherd.2019.05.059.
[66] S.E. Brika, Influence of particle morphology and size distribution on the powder flowability and laser powder bed fusion manufacturability of Ti-6Al-4V alloy, Additive Manufacturing. (2020) 16.
[67] S. Bakrani Balani, F. Chabert, V. Nassiet, A. Cantarel, Influence of printing parameters on the stability of deposited beads in fused filament fabrication of poly(lactic) acid, Additive Manufacturing. 25 (2019) 112–121. https://doi.org/10.1016/j.addma.2018.10.012.
[68] L. Waalkes, J. Längerich, F. Holbe, C. Emmelmann, Feasibility study on piston-based feedstock fabrication with Ti-6Al-4V metal injection molding feedstock, Additive Manufacturing. 35 (2020) 101207. https://doi.org/10.1016/j.addma.2020.101207.
[69] D.A. Anderegg, H.A. Bryant, D.C. Ruffin, S.M. Skrip, J.J. Fallon, E.L. Gilmer, M.J. Bortner, In-situ monitoring of polymer flow temperature and pressure in extrusion based additive manufacturing, Additive Manufacturing. 26 (2019) 76–83. https://doi.org/10.1016/j.addma.2019.01.002.
[70] C.W. Gal, J.W. Oh, G.W. Song, D.S. Shin, S.J. Park, Rheological and thermal debinding behaviors of silicon nitride in powder injection molding, Ceramics International. 45 (2019) 16982–16991. https://doi.org/10.1016/j.ceramint.2019.05.247.
[71] F. Cuomo, S. Iacovino, G. Cinelli, M.C. Messia, E. Marconi, F. Lopez, Effect of additives on chia mucilage suspensions: A rheological approach, Food Hydrocolloids. 109 (2020) 106118. https://doi.org/10.1016/j.foodhyd.2020.106118.
[72] T. Honek, B. Hausnerova, P. Saha, Temperature Dependent Flow Properties of Powder Injection Moulding Compounds, Applied Rheology. 12 (2002) 72–80. https://doi.org/10.1515/arh-2002-0004.
[73] Y. Li, B. Huang, X. Qu, Viscosity and melt rheology of metal injection moulding feedstocks, Powder Metallurgy. 42 (1999) 86–90. https://doi.org/10.1179/pom.1999.42.1.86.
[74] M.P. Serdeczny, R. Comminal, Md.T. Mollah, D.B. Pedersen, J. Spangenberg, Numerical modeling of the polymer flow through the hot-end in filament-based material extrusion additive manufacturing, Additive Manufacturing. 36 (2020) 101454. https://doi.org/10.1016/j.addma.2020.101454.
[75] G. Schramm, A practical approach to Rheology and Rheometry, 2nd ed., D-76227 karlsruhe, Dieselstrasse, 2000.

Appendix A: Powder flow tests and Additive Manufacturing Suitability (or AMS) indicator

To develop a powder-filled composite, it is necessary to select the right batch of powder to use and therefore to know its flow properties. One reason is that low flowability powders can generate defects in the filled composite [58].

The FT4 Powder Rheometer (Freeman Technology, Malvern, UK) provides the flow properties of powders assessed by various tests [59]; The standard dynamic tests, aeration testing and shear testing are automated with no operator involvement other than sample preparation [60]. Seven different experiments were performed and the measurements were repeated five times for each test.

Bulk density measurements: The conditioned bulk density, denoted ρ_c, is the conditioned initial density of the powder bed. It is calculated as the ratio of the split weight divided by split volume.

Dynamic downwards tests: This test measures the powder flow energy and takes place in seven cycles where each of them corresponds to one entry of the rotating blade into the powder bed and then to one exit. While the Basic Flowability Energy, denoted *BFE*, is measured during the downwards motion of the blade (confined regime), the Specific Energy, denoted *SE*, is determined when the blade moves upwards through the powder. The value of *BFE* is the energy needed to displace a conditioned powder during downwards testing and corresponds to the energy value of the 7th cycle of the mixer blade in **Fig. 3**a. The Stability Index, denoted *SI*, is the factor by which the measured flow energy changes during the 7 repeated downwards motion of the blade, so that [61]

$$SI = \frac{Energy\ test\ 7}{Energy\ test\ 1} \tag{5}$$

Finally, this test ends with the measurement of the flow energy of the powder when the flow rate (or mixer blade speed) is gradually reduced by a factor of ten. The Flow Rate Index, denoted *FRI*, is then introduce as the following ratio [61]

$$FRI = \frac{Energy\ test\ 11}{Energy\ test\ 8} \tag{6}$$

where "test 11" correspond to a mixer blade speed ten times smaller than "test 8".

Dynamic upwards tests: This test measures the flow energy of the powder corresponding to the exit of the rotating blade in the powder bed which is unconsolidated in its upper part, i.e. in a stress-free state. Due to the predominance of gravity in this test, the flow energy is expressed as Specific Energy mJ/g, denoted *SE,* to compensate for the variation in powder densities being compared [61]

$$SE = \frac{\frac{Up\ energy\ cycle\ 6 + Up\ energy\ cycle\ 7}{2}}{Split\ mass} \tag{7}$$

where the "Up energy" refers to the energy measured on the upward rotation of the mixer blade.

Compressibility test: To determine the powder's ability to be compressed, this test uses a porous piston to apply levels of normal stress to the sample while measuring its volume change. The compressibility of a powder is the percentage change in volume after compression. Compressibility Index, denoted *CI* index, is then introduced as the ratio between the initial density ρ_c and the final density for a given normal pressure [62].

Permeability test: To determine the capacity of the powder to be crossed by a flow of air, this test measures the Pressure Drop, denoted PD, across the powder bed while the applied normal pressure was varied and the air velocity through the bed was maintained constant at 2 mm/s (see [60] for the methodology).

Aeration test: This test measures powder flow sensitivity as a function of the air flow rate. It is similar to the stability and flow rate tests as it involves measuring the blade resistance in the powder bed using the same method defined previously as [63]. The flow energy recorded at the highest air velocity corresponds to powder-specific Aeration Energy, denoted *AE*.

Shear test: This test characterises the shear behaviour of the consolidated powder. In a rotating cell, the shear stress, caused by the friction of the powder against the walls of the cell, is measured as a function of the imposed normal stress in the shear cell [64]. It allows the measurement of several parameters of the powder particularly the cohesion coefficient, denoted *c*, defined as the shear stress corresponding to zero normal stress. In practice, it is obtained from the shear stress versus the applied normal stress curve and then extrapolated to zero [65].

The data collected by these tests allows the overall quality of powder flow to be qualified with the Additive Manufacturing Suitability (or AMS) indicator, whose general expression is given by Eq. (8). Brika et al. [66] used this AMS indicator to estimate the level of powder compatibility with the laser melting process on a powder bed. This indicator is used in this work as a factor of powder compatibility with the additive manufacturing process where a lower value will indicate better powder flow. It is defined by the sum of several factors normalised by the maximum value of the powder batch studied, such that

$$AMS = \left(\frac{1/\rho_c}{(1/\rho_c)_{max}} + \frac{BFE}{BFE_{max}} + \frac{SI}{SI_{max}} + \frac{FRI}{FRI_{max}} + \frac{SE}{SE_{max}} + \frac{CI}{CI_{max}} + \frac{PD}{PD_{max}} + \frac{AE}{AE_{max}} + \frac{c}{c_{max}}\right)/9 \quad (8)$$

where ρ_c, BFE, SI, FRI, SE, CI, PD, AE, and c denote the bulk density, stability index, basic flowability energy, specific energy, flow rate index, compressibility index, pressure drop, aeration energy, and cohesion coefficient, respectively.

With this definition, the lowest value of AMS will tend to select the powder with the highest bulk density ρ_c and lowest value of the other parameters, i.e. BFE, SI, FRI, SE, CI, PD, AE, and c.

Appendix B: Characterisation and modelling of shear viscosities

In this appendix, rheological characterizations of the different constituents of the binder, the binder and the composite are performed at different temperatures. A complete modelling of the shear stress as a function of the shear rate, then, simplified models are proposed to make studies of influence. The choice of the printing parameters of the composite, such as its shear rate and its nozzle temperature, are discussed. Finally, a third method is presented to confirm the highest powder loading in the F1 composite obtained in section 3.

B.1. Rheological characterizations

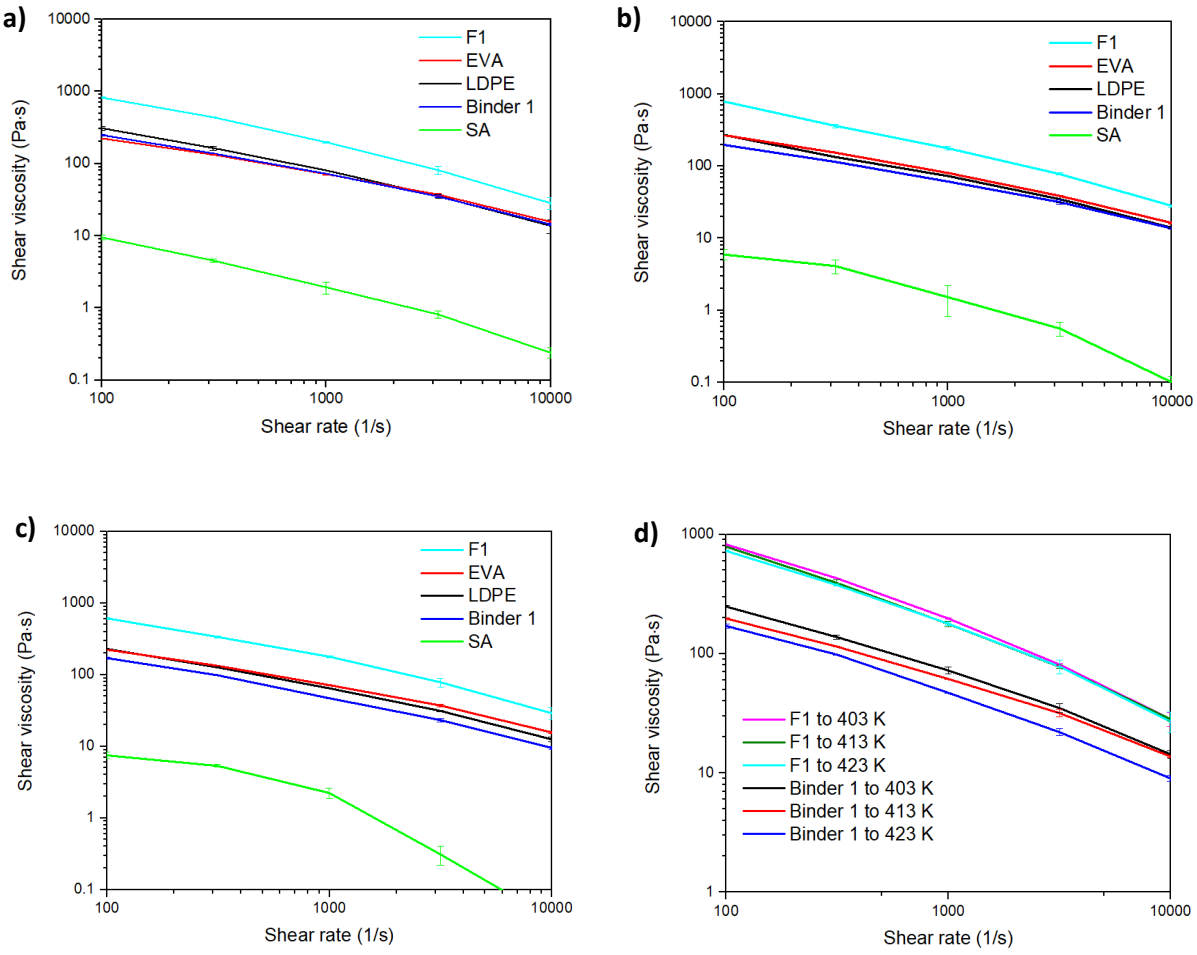

Fig. 13. Double Log plot of the evolution of shear viscosity versus shear rate for SA, pure polymers, binder 1, and F1 composite at a temperature of a) 403 K, b) 413 K, c) 423 K, and, d) binder 1 and F1 composite at 403, 413, and 423 K.

Fig. 13a–d shows shear viscosity as a function of shear rate for each of the constituents of Binder 1 (LDPE, EVA and SA), Binder 1, and F1 composite for different temperatures above their melting

point. All virgin materials (except for SA) have medium shear viscosity between 200 and 1000 Pa·s, which corresponds to the range of polymer EAM [67]. **Fig. 13**d shows, on the one hand, that the shear viscosity decreases with the shear rate which is typical of a pseudo-plastic behaviour of the binder and its composite [68] and, on the other hand, that the viscosity of the binder decreases with the increase in its temperature, namely its thermo-dependence, while that of the F1 composite remains constant.

B.2. Complete model of shear viscosity

Dimitri et al. [25] proposed a complete model of shear viscosity, denoted η, with the effects of temperature T, shear rate $\dot{\gamma}$, and volume fraction of powder φ, such as:

$$\eta(T,\dot{\gamma},\varphi) = \left[exp\left(\frac{E_a}{R.T}\right)\right].\eta_0\left[1+(\lambda\dot{\gamma})^a\right]^{\left(\frac{n-1}{a}\right)}.\left(\frac{\varphi_{max}}{\varphi_{max}-\varphi}\right)^m \quad (9)$$

where E_a, R, η_0, λ, a, n, φ_{max} and m denotes the activation energy, perfect gas constant, viscosity at the reference temperature when $\dot{\gamma}=0$, relaxation time, the width of the transition between the Newtonian regime and the power law, the power-law exponent, the maximum volume ratio of powder, and the power exponent of the effect of the volume fraction of powder, respectively.

The most influential parameters are E_a, n, and m, which provide pertinent information regarding the rheological behaviour of the materials. All the parameters involved in Eq. (9) have been identified from the experimental results. E_a was determined from the shear viscosity versus temperature curve and the shear rate η_0, the relaxation time λ and the power-law exponent n were identified based on the relationship between the shear viscosity and shear rate. Finally, the power exponent m was deduced from the relationship between the shear viscosity and the volume fraction of powder, in other words, by using the simplified modellings presented below.

B.3. Influence of temperature on shear viscosity

According to Eq. (9), the dependence of the shear viscosity η on temperature T alone reduces to a simple Arrhenius law such as [69]:

$$\eta(T) = B\ exp\left(\frac{E_a}{R\cdot T}\right) \quad (10)$$

where B denotes the shear viscosity at a given shear rate and volume fraction of powder and the other parameters are the same as those used in Eq. (9).

The activation energy E_a determines the sensitivity of the material viscosity to temperature. A high value of E_a will contribute to a large change in the shear viscosity of the material affected by temperature [70, 71] while a low value will avoid stress concentrations that could cause cracks in the final 3D printed part [72].

To determine the shear rate value $\dot{\gamma}$ during the printing process, the same method as Balani et al. [67] was used. It was given by the velocity based on the radius of the internal nozzle diameter, which is taken from its inner wall to obtain its maximum value, such that: $\dot{\gamma} = \left(\frac{du}{dr}\right)_{r=R} = \frac{3\,n+1}{n\,R}\,\bar{V}$ where $\bar{V}$ is the average velocity of the polymer at the nozzle inlet, R is the internal nozzle radius, and n is the power-law exponent. $\bar{V}$ is given by the expression: $\bar{V} = \frac{4\,f}{4\,\pi\,R^2}\left(w\,h + \frac{\pi\,h^2}{4}\right)$ where h is the height of the deposited filament, f is the printing speed, and w is the width of the deposited filament. The application of this method conducts to a shear rate of $\dot{\gamma} = 313$ s^{-1} with our equipment and material.

Table 10

Parameters of Eq. (10) identified on the experimental data presented in **Fig. 13** for each constituent of binder 1, binder 1 and F1 composite for a shear rate of 313 s^{-1} and with R = 8.314 J·K^{-1}·mol^{-1}.

Material	E_a **(kJ·mol^{-1})**	B **(Pa·s)**
LDPE	23.64	0.76
EVA	25.89	0.08
SA	12.07	0.09
Binder 1	23.91	0.11
F1 composite	23.26	2.46

Using a linear regression from **Fig. 13** plotted in log-log for the shear rate of 313 s^{-1}, the parameters of Eq. (10) are identified and given in **Table 10**.

The activation energy value of composite F1 remains low and is of the same order of magnitude as that reported in the literature (see [73]). It is known that polymer materials with a high viscosity (involving low activation energy) in the range of shear rates between 10 s^{-1} and 10^3 s^{-1} are perfectly suited to the EAM process to maintain the final shape of the manufactured part [74].

Therefore, to have a high viscosity value of the F1 composite, its printing temperature of 403 K is retained for further printing.

B.4. Influence of the shear rate on viscosity and third determination of the CSL ratio

The conventional rheological model in power-law is obtained after a simplification of Eq. (9). The combined effects of a shear rate $\dot{\gamma}$, of temperature T and volume fraction of powder φ on the shear viscosity η of the composite are then such as:

$$\eta(T,\dot{\gamma},\varphi) = K(T,\varphi)\,(\dot{\gamma})^{n-1} = K_0\,.\left[exp\left(\frac{E_a}{R.T}\right)\right].(\dot{\gamma})^{n-1}.\left(\frac{\varphi_{max}}{\varphi_{max}-\varphi}\right)^{(m)} \quad (11)$$

where K denotes the flow consistency index and the other parameters are the same as those used in Eq. (9).

Fig. 14a shows the shear viscosity of the F1 composite for different volume fractions of powder at 403 K as a function of the shear rate presented in a double logarithmic plot. The shear viscosity decreases with the shear rate, indicating a pseudo-plastic or a non-Newtonian behaviour of the composite [75]. A linear fitting of these experimental curves is also presented in this **Fig. 14**a.

A third method used to determine the critical solid powder loading (or CSL) consists in analysing the evolution of the power-law exponent fitting the viscosity of the composite according to its volume fraction of powder [43]. **Fig. 14**b shows the evolution of these identified values of exponent n as a function of the volume fraction of powder and highlights an inflection point at the CSL ratio of about 50 vol.% for $n = 0.26$ which corresponds to the homogeneous-inhomogeneous transition of the F1 composite. The obtained value of n is less than 1, revealing in addition a pseudo-plastic behaviour with a shear-thinning fluid.

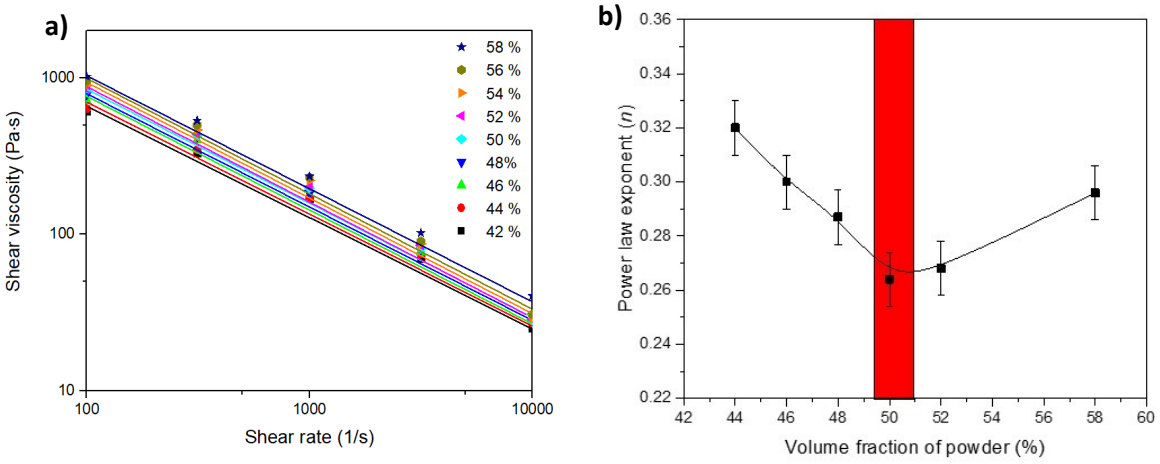

Fig. 14. F1 composite at 403 K: a) Double Log plot of their shear viscosities versus shear rate for different volume fractions of powder, b) Evolution of the power-law exponent *n* identified versus volume fraction of powder. (Points: experiment data, and, line: fitting curve).

B.5. Identification of the complete shear viscosity model

To predict the rheological behaviour of F1 composite versus temperature, shear rate, and volume fraction of powder, the parameters of the complete model are identified and are summarised in **Table 11**. **Fig. 15** shows the discrepancy between the shear viscosity model and the experimental data for the F1 composite at 403 K. The predicted curves exhibited the same trend as the experimental data with a difference $\Delta\eta$ of around 186 Pa·s at 313 s^{-1}. In conclusion, the complete rheological model provides a good prediction of the experimental data of the composite around the selected operating point (i.e. shear stress of 313 s^{-1} and temperature of 403 K), as shown in **Fig. 15**.

Table 11

List of the different identified parameters of the complete model for the F1 composite at 403 K.

Model	$\dot{\gamma}$ **(s^{-1})**	E_a **($kJ \cdot mol^{-1}$)**	η_0 **(Pa·s)**	K **(Pa·s)**	λ **(s)**	a **(1)**	n **(1)**	m **(1)**	φ_{max} **(vol.%)**
Complete model (Eq. (9))	100	23.26	1103	-	0.1	2	0.26	1.42	61
	313							1.31	
	999							1.27	
	3162							1.21	
	9999							1.01	

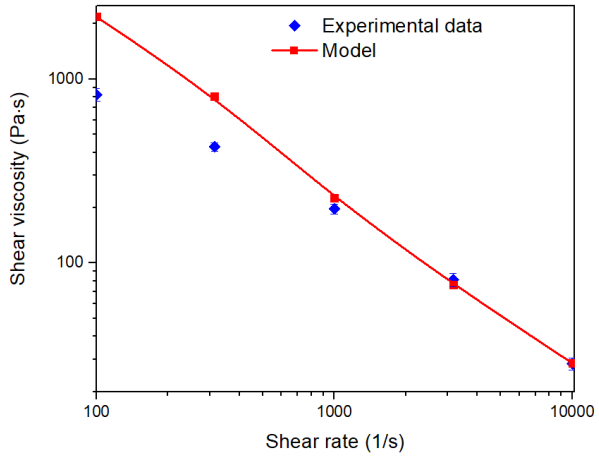

Fig. 15. Shear viscosity of the F1 composite versus the shear rate at 403 K: experimental points and fitting curves with the complete model.